

Spin period evolution of GX 1+4

A. González-Galán¹, E. Kuulkers², P. Kretschmar², S. Larsson^{3,4}, K. Postnov⁵, A. Kochetkova⁵, and M.H. Finger^{6,7}

¹ Department of Physics, Systems Engineering and Sign Theory, University of Alicante, P.O. Box 99 E-03080 Alicante, Spain
e-mail: anagonzalez@ua.es

² European Space Agency, European Space Astronomy Centre, P.O. Box 78, 28691, Villanueva de la Cañada, Madrid, Spain

³ Department of Astronomy, Stockholm University, SE-106 91 Stockholm, Sweden

⁴ The Oskar Klein Centre for Cosmoparticle Physics, AlbaNova, SE-106 91 Stockholm, Sweden

⁵ Sternberg Astronomical Institute, 119992, Moscow, Russia

⁶ National Space Science and Technology Center, 320 Sparkman Drive, Huntsville, AL 35805, USA

⁷ Universities Space Research Association, 6767 Old Madison Pike, Suite 450, Huntsville, AL 35806, USA

Received; accepted

ABSTRACT

Aims. We aim both to complement the existing data on the spin history of the peculiar accreting X-ray pulsar GX 1+4 with more past and current data from BeppoSAX, INTEGRAL, and Fermi and to interpret the evolution in the framework of accretion theory.

Methods. We used source light curves obtained from BeppoSAX/WFC and INTEGRAL/ISGRI to derive pulse periods using an epoch-folding analysis. Fermi/GBM data were analysed by fitting a constant plus a Fourier expansion to background-subtracted rates, and maximizing the Y_2 statistic. We completed the sample with hard X-ray light curves from Swift/BAT. The data were checked for correlations between flux and changes of the pulsar spin on different timescales.

Results. The spin-down of the pulsar continues with a constant change in frequency, i.e., an apparently accelerating change in the period. Over the past three decades, the pulse period has increased by about $\sim 50\%$. Short-term fluctuations on top of this long-term trend do show anti-correlation with the source flux. Possible explanations of the observed long-term frequency and its dependence on flux are discussed.

Key words. accretion, accretion discs - X-rays: binaries - stars: pulsars: individual (GX 1+4)

1. Introduction

Accreting X-ray pulsars are highly magnetized neutron stars in a binary system, which accrete matter from their companion star. The mass transfer can take place via Roche-Lobe overflow for low mass X-ray binaries (LMXBs), strong stellar winds for giant stars in high mass X-ray binaries (HMXBs), or the Be emission mechanism for Be X-ray binaries. These accreting pulsars radiate predominantly in the X-ray band, and the radiation is modulated by the stellar rotation of the pulsar. For a review of this subject, see e.g., Nagase (1989).

Since the discovery of the first accreting X-ray pulsars, Cen X-3 (Giacconi et al. 1971), GX 1+4 (Lewin et al. 1971), and Her X-1 (Tananbaum et al. 1972), the pulse periods of well-established accreting X-ray pulsars have been monitored more or less regularly with a wide variety of high-energy observatories. Early observations mainly found sources being spun up, which was easily explained by the acceleration through the angular momentum of accreted matter. Further investigations have demonstrated a wide variety in the pulse-period evolution, with some sources best described by a random walk, others showing clear secular changes. Various models (e.g., Ghosh & Lamb 1977; Wang 1987; Lovelace et al. 1995) have been proposed to explain the observed behaviour.

GX 1+4 was discovered in 1970 by a balloon X-ray observation at energies above 15 keV showing pulsations with a period of about two minutes (Lewin et al. 1971). During the 1970s, it was one of the brightest X-ray sources in the

Galactic centre region and was globally spinning up strongly (e.g., Doty et al. 1981; Warwick et al. 1981; White et al. 1983; McClintock & Leventhal 1989). In the early 1980s the source went through a low state in X-ray flux and remained undetectable, because at least two orders of magnitude below the previously observed levels (Hall & Davelaar 1983; Mukai 1988). When the source was detected again it had undergone a torque reversal (Makishima et al. 1988), and ever since it has been generally spinning down strongly, see Appendix A.

The optical counterpart of GX 1+4 was discovered by Glass & Feast (1973) as the infrared source V2116 Oph. The optical composite emission spectrum of the proposed counterpart indicated that the object was almost certainly a binary system, consisting of a symbiotic red giant and a much hotter source (Davidsen et al. 1977). Chakrabarty & Roche (1997) confirm the optical companion to be V2116 Oph. More recently, infrared observations have indicated a mass of about $1.2 M_{\odot}$ for the M giant star (assuming a mass of about $1.35 M_{\odot}$ for the neutron star), implying that the M giant star is a first ascent giant that does not fill its Roche Lobe (Hinkle et al. 2006). Therefore, GX 1+4 is a LMXB that is capturing the stellar wind of its M6III companion (Chakrabarty & Roche 1997; Hinkle et al. 2006). GX 1+4 is the first and the prototype of the small but growing subclass of accreting X-ray pulsars called symbiotic X-ray binaries (SyXB), by analogy with symbiotic stars, in which a white dwarf accretes from the wind of an M-type giant companion (e.g., Masetti et al. 2006, 2007; Corbet et al. 2008).

Cutler et al. (1986) proposed an orbital period of about 304 days based on variations in the pulse period of the neutron star of

GX 1+4 during the spin-up phase in the 1970s. Other authors (e.g., Pereira et al. 1999; Braga et al. 2000) have supported this using observations from 1991 to 1998, when the source was already in its long-term spin-down phase (see also Fig. 6). More recently, infrared observations have shown a 1161-day period single-line spectroscopic binary orbit, which excludes the 304-day period as the orbital period (Hinkle et al. 2006). GX 1+4's X-ray light curves show strong variability on a timescale of days to years but with no modulation on either the optical 1161-day orbital period or the previously reported 304-day X-ray (e.g., Naik et al. 2005; Corbet et al. 2008).

Based on X-ray and infrared observations, Chakrabarty & Roche (1997) have constrained the distance range to the system as between 3 and 15 kpc, depending on the evolutionary state of the red giant. For a first-ascent giant branch star (Chakrabarty & Roche 1997; Hinkle et al. 2006), the estimates have narrowed down to 3-6 kpc (Chakrabarty & Roche 1997). The distance estimate by Hinkle et al. (2006), 4.3 kpc, is consistent with this. Thus, in spite of its position in the sky (see, e.g., Predehl et al. (1995)), GX 1+4/V2116 Oph is clearly not an object associated with the centre of the Milky Way (Hinkle et al. 2006). Hinkle et al. (2006), however, do not provide any uncertainty on the distance, and an uncertainty of 0.1 kpc, based on the precision of their estimate, seems to be too precise. They do provide an uncertainty in the effective temperature of the giant star (± 200 K) and its radius ($+42, -30 R_{\odot}$), which would give a range in the absolute luminosity, and therefore, an uncertainty in the distance may be estimated, while taking the interstellar extinction into account. Estimates of the latter, in terms of $E(B - V)$, have been reported by various authors: 1.62 ± 0.19 (Chakrabarty & Roche 1997), 1.7 ± 0.4 (Davidsen et al. 1977), 2.1 ± 0.1 (Jablonski et al. 1997), 2.30 ± 0.06 (Shahbaz et al. 1996).¹ This rather wide range in extinction has a strong effect on the uncertainty in the distance, i.e., about a few kpc. With the mean observed V-band magnitude, $V = 18.40 \pm 0.03$ mag, $E(B - V) = 1.62 \pm 0.19$ or, equivalently, $A_V = 5.0 \pm 0.6$ (Chakrabarty & Roche (1997), and assuming an absolute magnitude M_V of about -0.25 for an M6III star (The et al. 1990), we derive a distance of 5.4 ± 1.6 kpc. A higher reddening value, for example, of $E(B - V) = 2.30 \pm 0.06$ or, equivalently, $A_V = 7.1 \pm 0.2$ (Shahbaz et al. 1996) would lead to a distance of 2 ± 0.2 kpc. We, therefore, conclude that Chakrabarty & Roche (1997) give a more realistic estimate than Hinkle et al. (2006) and that the uncertainty on the distance is about 1.5 kpc. In this paper we adhere to the distance estimate of 4.3 kpc.

Currently, there is no well established value for the magnetic field of GX 1+4. Assuming the standard accretion-disc theory (Ghosh & Lamb 1979a,b; Wang 1987), the magnetic field has been estimated to be $B \sim 10^{13} - 10^{14}$ G (e.g., Dotani et al. 1989; Mony et al. 1991; Cui & Smith 2004), which is among the largest measured for any accreting X-ray pulsar. There have been marginal reports of cyclotron scattering resonance features (CRSFs) in the X-ray spectra, which points to a value of $B \sim 10^{12}$ G for the magnetic field, i.e., up to two orders lower (e.g., Rea et al. 2005; Ferrigno et al. 2007).

GX 1+4's unusual long-term spin behaviour has attracted considerable interest for many years. Studying the pulse-period evolution in an accreting X-ray pulsar and relating it to, e.g., the luminosity changes, allows testing theoretical models and gaining insight into the interaction between the pulsar's magnetosphere

and the accreted matter. In this paper we extend the investigation of the spin-period history of GX 1+4 with new observations obtained by BeppoSAX, INTEGRAL, and Fermi. The available measurements of the pulse period of GX 1+4 span a period of about 40 years. This gives us a unique insight in the pulse period evolution of this SyXB. Apart from GX 1+4 still spinning down overall, we find irregular trends on top of this evolution. We correlate these features with the high-energy flux of the system using the same observations as well as those obtained with Swift, and provide an explanation for the spin history seen.

2. Observations

2.1. CGRO

The Compton Gamma-Ray Observatory, CGRO, was a NASA mission launched in April 1991 (Gehrels et al. 1993) and operative until June 2000 (Kaneko et al. 2006). The Burst And Transient Source Experiment, BATSE, onboard CGRO was a sensitive all-sky instrument that consisted of eight uncollimated Na I scintillation detectors at the corners of the spacecraft. It covered a broad energy range from 15 keV to 100 MeV. Each detector module contained a large-area detector (LAD) optimized for sensitivity and directional response and a spectroscopy detector (SD) optimized for broad energy coverage and energy resolution (Fishman et al. 1992).

BATSE monitored pulse frequencies and X-ray pulsed fluxes for roughly half of the known X-ray pulsars (Nelson et al. 1997b). GX 1+4 results from this survey are publicly available in the form of pulse source histories covering the energy range from 20 keV to 50 keV and daily frequencies from April 1994 to May 1997.²

2.2. BeppoSAX

The X-ray satellite "Satellite per Astronomia X", BeppoSAX, was an Italian/Dutch mission launched in April 1996 and operated until April 2002, then deorbited in April 2003. It covered more than three decades in energy (about 0.1 to 300 keV) with relatively good energy resolution, and provided imaging capabilities in the range of 0.1-10 keV. Together with the Wide-Field Camera's (WFCs), the broad-band Narrow-Field Instruments (NFIs) provided the opportunity to study the broad-band behaviour of several classes of X-ray sources (Boella et al. 1997). The WFCs (Jager et al. 1997) were two identical coded-aperture instruments onboard BeppoSAX. The field of view was $40^{\circ} \times 40^{\circ}$ full width zero response (FWZR), the angular resolution $5'$ full width half maximum (FWHM) and the source-location accuracy was generally better than $1'$ (99% confidence). The detectors were sensitive to the energy range 2 to 28 keV. The WFCs pointed in opposite directions with respect to each other and perpendicular to the NFIs. The pointing directions of the WFCs were usually governed by the observations of the NFIs. However, a few dedicated campaigns on the Galactic bulge region were performed by the WFCs (see, e.g., in't Zand et al. 2004). We analysed WFC data obtained from August 1998 to August 2000.

2.3. INTEGRAL

INTEGRAL (Winkler et al. 2003) is an ESA scientific mission that was launched in October 2002. It is dedicated to spec-

¹ The observed optical extinction is mainly attributed to interstellar dust, while the variable X-ray absorption is possibly due to the wind of the giant star, see Chakrabarty & Roche (1997).

² See <ftp://legacy.gsfc.nasa.gov/compton/data/batse/pulsar/histories/>.

Table 1. INTEGRAL observation periods (OP)

OP	Start Date	End Date	MJD	Effective Exposure
	(UT)			
1	2005/02/18	2005/04/19	53419-53479	258 ks
2	2005/08/16	2005/10/26	53598-53669	377 ks
3	2006/08/9	2006/04/21	53775-53846	276 ks
4	2006/08/13	2006/10/23	53963-54031	461 ks
5	2007/02/15	2007/04/21	54146-54211	853 ks
6	2007/08/19	2007/10/14	54331-54387	599 ks
7	2008/02/11	2008/04/20	54507-54576	225 ks

troscopy and imaging of celestial γ -ray sources in the energy range between 15 keV and 10 MeV with simultaneous monitoring in the X-ray and optical energy ranges. Several instruments are on board: SPectrometer onboard INTEGRAL (SPI), Imager on Board INTEGRAL Satellite (IBIS), Joint European Monitor X-rays (JEM-X) and Optical Monitoring Camera (OMC). The former three instruments all collect photons through wide-field coded masks.

IBIS (Ubertini et al. 2003) comprises two detector planes. The field of view is $29^\circ \times 29^\circ$ (FWZR) and the angular resolution $12'$ (FWHM). In this paper we only used data collected with one of its detectors: the INTEGRAL Soft Gamma-Ray Imager (ISGRI). It is sensitive in the ≈ 15 keV to 1 MeV range (Lebrun et al. 2003).

The INTEGRAL Galactic bulge monitoring programme started in February 2005 and was initiated to monitor the Galactic bulge region on a regular basis in mainly the hard X-ray band. One complete hexagonal dither pattern (7 pointings of ≈ 1800 s each) is performed during each INTEGRAL orbit around the Earth, (roughly every 3 days), whenever the bulge region is visible by INTEGRAL: twice per year for a total period of about four months (see Kuulkers et al. 2007).

We analysed the ISGRI data from observations of the Galactic bulge monitoring programme between February 2005 and April 2008. These observations span several periods, see Table 1. Each time span is referred to as observation period, or OP for short.

2.4. Swift

Swift is a NASA mission that was launched in November 2004 (Gehrels et al. 2004). The Burst Alert Telescope (BAT; Barthelmy et al. 2005) onboard Swift is a coded-aperture imager with a very wide field of view of about 2 steradians, which operates in the 15–150 keV band. The BAT angular resolution is $22'$ (FWHM).

The BAT continually monitors the sky with more than about 70% of the sky observed on a daily basis. Results from this survey are publicly available in the form of light curves covering the 15–50 keV energy band on two timescales: a single Swift pointing (≈ 20 min) and the weighted average for each day.³ We used the daily average light curve for GX 1+4 to study its long-term hard X-ray flux behaviour.

2.5. Fermi

The Fermi Gamma-ray Space Telescope, formerly Gamma-ray Large Area Space Telescope (GLAST), is a NASA mission that was launched in June 2008. It has two instruments on board: the

Large Area Telescope (LAT) and the Gamma-ray Burst Monitor (GBM). Fermi is dedicated to measuring the cosmic gamma-ray flux in the energy range 20 MeV to > 300 GeV, with supporting measurements for gamma-ray bursts (Ritz et al. 2009).

Since 2008 August 12 GX 1+4 has been continuously monitored by the GBM (Meegan et al. 2009). The GBM is an all-sky instrument sensitive to X-rays and gamma rays with energies between ~ 8 keV and ~ 40 MeV. Timing analysis is carried out with channels 1 and 2 of the NaI detector CTIME data (12–50 keV, 0.256 s time resolution).

We analysed GBM data from August 2008 to February 2010.

3. Data analysis

For INTEGRAL/ISGRI, the data were reduced using version 7 of the INTEGRAL off-line analysis software (OSA 7), distributed by the INTEGRAL Science Data Centre (ISDC; Courvoisier et al. 2003). Each data set in a revolution (about 13 ks long) has been analysed in the energy range between 20 keV and 40 keV, following the steps described in the IBIS Analysis User Manual (version 6.0). We used the *ii_Light* tool to obtain light curves with a time bin of 10 s and barycentric correction was applied. The source BeppoSAX/WFC flux was reconstructed in the 2–25 keV bandpass with a time resolution of 2 s. Period determinations for both the INTEGRAL/ISGRI and BeppoSAX/WFC data have been done for segments of the light curve using an epoch-folding analysis (Larsson 1996). The data for such a segment is folded at a number of different test periods, and for each period, the χ^2 over the resulting pulse profile is computed. A best-fit period is determined by fitting a template function describing how χ^2 should vary with a test period. The template function takes the time sampling of the data into account and, in an iterative procedure, the pulse shape of the oscillation. Uncertainties are estimated by Monte Carlo simulations. A set of synthetic pulse light curves with the same time sampling and noise level as the data are created and analysed. The distribution of determined periods for these simulations is used as a measure of period uncertainty. Pulse period determination for INTEGRAL/ISGRI data was possible for most hexagonal pattern observations. From a total of 128 hexagonal dither patterns it was possible to obtain 121 light curves (in 7 of these 128 observations the source was below the detection limit of the instrument) and to derive 93 pulse periods, which is $\sim 77\%$ of the detections. For 28 detections it was not possible to derive the pulse period because the source detection significance was lower than 14 and no clear maximum in the χ^2 distribution was found owing to the noise.

The analysis of the Fermi/GBM data is complicated by Fermi's continuously changing orientation. All intervals of CTIME data from the 12 NaI detectors are selected for analysis where the high voltage is on, excluding those containing high-voltage transients, phosphorescence events, rapid spacecraft slews, South Atlantic Anomaly induced transients, electron precipitation events, and gamma-ray bursts. Source pulses are then separated from the background by fitting the rates in all detectors with a background model and subtracting the best-fit model. This model includes bright sources and their changing detector responses (including Earth occultation steps), along with quadratic spline functions that account for the remaining long-term background trends. The spline models have statistical constraints on the changes in second derivative between spline segments to control the model stiffness. These fits are made jointly across detectors (with common bright source fluxes) but separately for each channel of the CTIME data. The residuals are then

³ <http://swift.gsfc.nasa.gov/docs/swift/results/transients/index.html>.

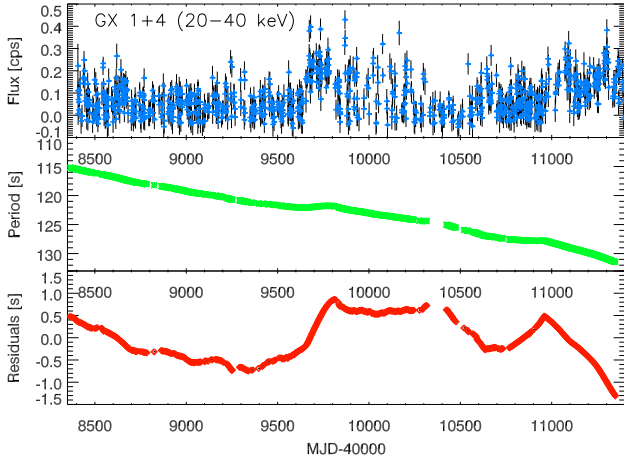


Fig. 1. *Top:* GX 1+4 CGRO/BATSE daily light curve in the energy range 20-40 keV. *Middle:* Pulse periods derived from CGRO/BATSE data, with the period increasing from top to bottom. *Bottom:* Residuals of the periods from a linear fit.

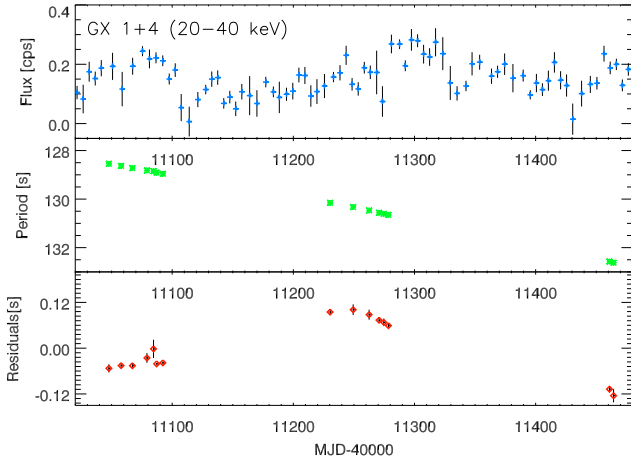


Fig. 2. *Top:* GX 1+4 CGRO/BATSE daily light curve in the energy range 20-40 keV. *Middle:* Pulse periods derived from BeppoSAX/WFC data. Note that the period increases from top to bottom. *Bottom:* Residuals of the periods from a linear fit.

summed over detectors with time-dependent weights that are proportional to the predicted (phase-averaged) count rates from the source. Short intervals (900s) of these combined residuals are then fitted with a constant plus a Fourier expansion to determine a pulse profile. The profiles are divided into four-day intervals, and the pulse frequency and mean profile are then determined in each interval with a search of pulse frequency for the maximum of the Y_n ($n = 2$) statistic (Finger et al. 1999). Y_n was formulated to find a pulse frequency from a series of pulse profiles, each represented by a finite Fourier expansion, so it accounts for possible frequency-dependent non-Poisson noise.

We did not apply Doppler corrections to the data, since the projected semi-major axis has not been measured with X-ray observations. The latter is mainly due to the high level of torque variability at low frequencies.

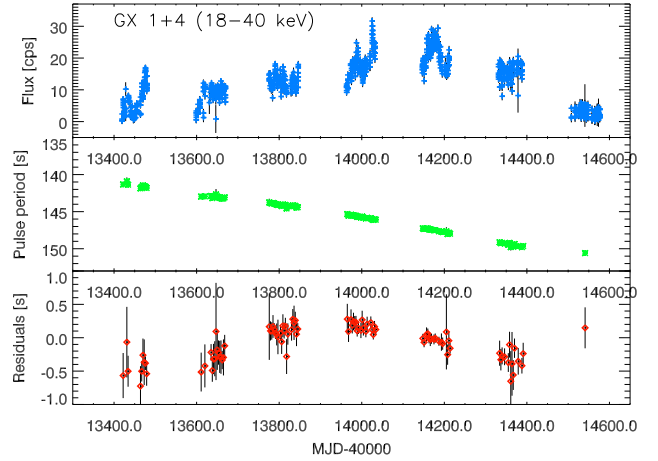


Fig. 3. *Top:* GX 1+4 INTEGRAL/ISGRI average flux per pointing in the energy range 18 to 40 keV. *Middle:* Pulse periods derived from INTEGRAL/ISGRI data. Note that the period increases from top to bottom. *Bottom:* Residuals from the pulse periods using a linear fit.

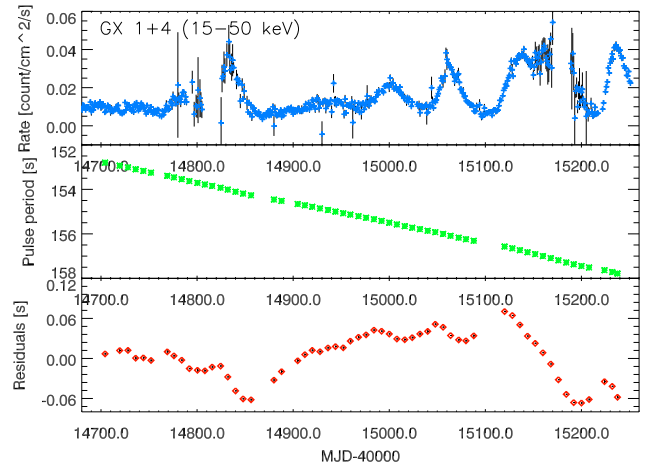


Fig. 4. *Top:* GX 1+4 Swift/BAT daily averaged light curve in the energy range 15–50 keV. *Middle:* Pulse periods derived from Fermi/GBM data, with the period increasing from top to bottom. *Bottom:* Residuals from the pulse periods using a linear fit.

4. Pulse period evolution

4.1. CGRO

The CGRO/BATSE data can be found in Fig. 1. The period increases in time with an almost linear trend, but with some fluctuations. A linear fit to these data resulted in a slope of $(5.61 \pm 0.03) \times 10^{-8}$ s/s with a Pearson r^2 value of 0.994. The deviations from this linear fit are shown in the bottom panel of Fig. 1. In this figure it is possible to observe a deviation from the linear fit of the spin period evolution around MJD 49700, where the neutron star spin-down rate decreases in coincidence with an increase in the X-ray flux. Overall, the deviations in the linear fit shown in the bottom panel of this figure are visually comparable to the variations in the X-ray flux shown in the upper panel of the same figure.

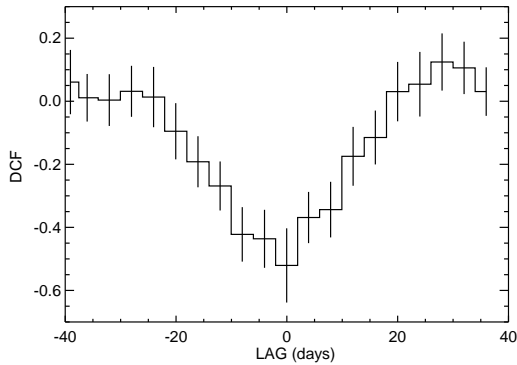


Fig. 5. The discrete correlation function (DCF), i.e., the correlation coefficient between the 15–50 keV X-ray flux and the pulse period change $\dot{\nu}$, as function of the time lag. The minimum near zero lag implies an anti-correlation between the pulse frequency derivative and X-ray flux.

4.2. BeppoSAX

The BeppoSAX/WFC pulse periods are shown in Fig. 2. The pulse period continues to increase with time. A linear fit to the pulse period as a function of time results in a slope of $(1.113 \pm 0.017) \times 10^{-7}$ s/s with a Pearson r^2 value of 0.998. The residuals from this linear fit are shown in the bottom panel of Fig. 2. The CGRO/BATSE X-ray pulsed flux contemporaneous to the WFC data is shown in the top panel of this figure. The sparsity of the pulse period measurements means we cannot see any clear correlations between the X-ray flux and the spin-period evolution in this data set.

4.3. INTEGRAL

The results using the INTEGRAL/ISGRI data are shown in Fig. 3. The pulse period increases with time with an almost linear trend. We find a slope of $(1.031 \pm 0.007) \times 10^{-7}$ s/s with a Pearson r^2 value of 0.995. As can be seen in the bottom panel of Fig. 3, the last point at MJD 54541 is only a marginal detection of the pulse period. Any linear fit not taking this last data point into account does not lead to a significantly different slope. The deviations from the linear fit not taking it into account the last data point are shown in the bottom of Fig. 3. In this data set there is a maximum for the deviations of the spin-period linear fit around MJD 53900, followed by a maximum for the X-ray flux around MJD 54100.

4.4. Fermi

The pulse period results using the Fermi/GBM data can be seen in the middle panel of Fig. 4. Again, the period evolution for GX 1+4 follows an almost linear trend with a slope of $(1.0697 \pm 0.0002) \times 10^{-7}$ s/s and a Pearson coefficient of $r^2 = 0.999$. The evolution of the Swift/BAT hard X-ray flux is shown at the top of this figure.

4.5. X-ray flux versus spin period

Theoretical models predict certain correlations between X-ray fluxes and pulse period evolution. For example, the complete and continuous data series in Fig. 1 led Chakrabarty et al. (1997) and Nelson et al. (1997a) to demonstrate for the first time a

negative correlation between spin-up rate $\dot{\nu}$ and X-ray luminosity. Motivated by this, we searched for correlations in the data shown in Fig. 4 which represents the most complete and continuous data series of period and fluxes. We calculated the discrete correlation function, DCF (see Edelson & Krolik 1988; Peterson et al. 1998), between $\dot{\nu}$, estimated over eight day bins, and the one-day binned Swift/BAT 15–50 keV flux. The DCF for the full MJD 54700–55240 time range (Fig. 5) shows a strong negative correlation at zero lag (-1.3 ± 2.6 days). Since the main uncertainty of the DCF is random correlation with erratic X-ray flickering in the light curve, we divided the data into four sections and computed the DCF for each. Strong anticorrelation (~ -0.6) was seen in the last two of these, and it was weaker (~ -0.3 to -0.4) in the first two sections. In all four the DCF minimum for lags between -40 and $+40$ days occurred close to, and was consistent with, no lag.

Comparing the instantaneous spin frequency derivative derived from the Fermi/GBM data with the flux simultaneously measured by the Swift/BAT monitor we find a dependence $-\dot{\nu} \propto F_x^{(0.30 \pm 0.07)}$. This is in line with the correlation of instantaneous spin-down torque with X-ray flux discovered by BATSE (Chakrabarty et al. 1997).

4.6. Long-term pulse period evolution

The long-term pulse period evolution of GX 1+4 is shown in Fig. 6. We combined all measurements that we are aware of from the literature with the pulse periods determined from BeppoSAX/WFC, INTEGRAL/ISGRI, and Fermi/GBM data as presented in the previous subsection. The main features in Fig. 6 are the well known switch from a strong spin-up to a spin-down trend in the 1980s and a continued spin-down slowly increasing in average \dot{P} over the years. The spin-down rate observed around 2004 was $\dot{P} \sim 10^{-8}$ s/s, while the spin-down trend observed in this work with INTEGRAL/ISGRI (2005–2008) and with Fermi/GBM (2009–2010) is $\dot{P} \sim 10^{-7}$ s/s, taking the spin-down measure in frequencies, the global evolution since the start of spin-down is described very well by a linear trend of $-0.1177(3)$ mHz/y as it is shown in the upper panel of Fig. 7. On top of these spin-down trends, irregularities are seen that have sometimes been proposed to correlate with the binary orbit (e.g., Pereira et al. 1999; Braga et al. 2000). (For a more detailed description see Section 5.1 and Appendix A). These irregularities are reflected in the middle panel of Fig. 7, but we note also that other apparent trend changes occur at times far from the predicted perigee passages.

5. Discussion

5.1. A retrograde disc in GX 1+4?

When GX 1+4 was discovered, the pulsar was spinning up, and the spin-up rate $\dot{\nu}$ was apparently correlated with the observed X-ray flux, which is usually interpreted as a direct measure of X-ray luminosity, hence mass accretion rate \dot{M} (e.g., Doty et al. 1981; Ricketts et al. 1982). This supported the idea that the period decrease is produced by accretion torques of a prograde disc around the neutron star (e.g., Ghosh & Lamb 1979b; Wang 1987).

Around 1983–1984 GX 1+4 entered a low X-ray luminosity state (Hall & Davelaar 1983; Mukai 1988), suggesting a large reduction in the mass accretion rate, and it started to spin down. Makishima et al. (1988) were the first to propose for GX 1+4 that a retrograde disc is formed around the neutron star by matter

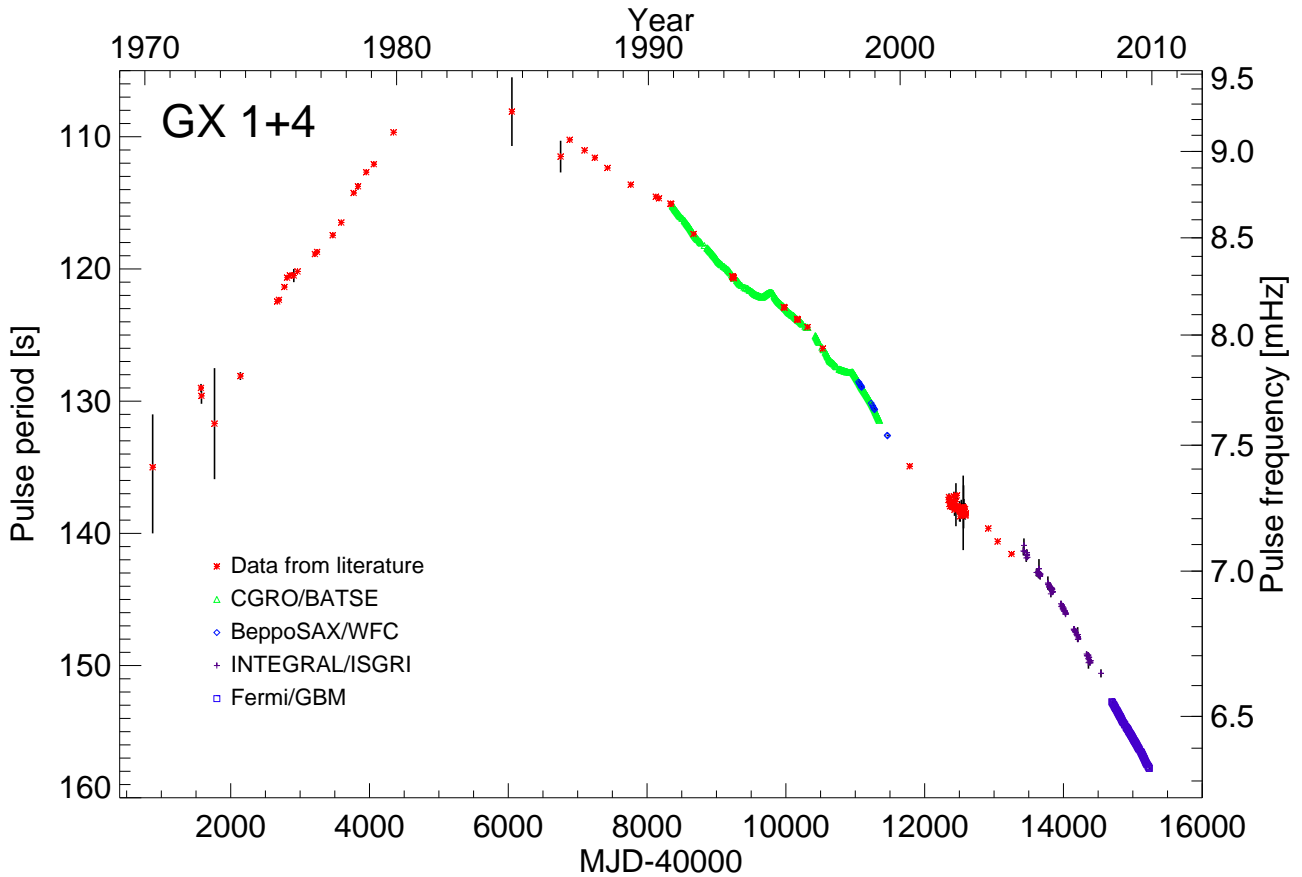


Fig. 6. The long-term pulse period evolution of GX 1+4, incorporating data from the literature and results of this work. See Table B.1 for data and references.

captured from the stellar wind of the M-giant companion of the pulsar, to explain the observed spin-down. Since then, this retrograde disc hypothesis has been supported by several authors (e.g., Dotani et al. 1989; Chakrabarty et al. 1997; Nelson et al. 1997a) for different reasons. One of the arguments in favour of the retrograde disc hypothesis is related to the magnetic field. To explain the spin-down of a pulsar accreting from a prograde standard disc (see e.g., Ghosh & Lamb 1977, 1979a,b; Wang 1987), the neutron star must be rotating very near its equilibrium spin period. The pulsar should then be in a quasi-equilibrium state, and GX 1+4 consequently has the strongest known magnetic field of any neutron star ($B \sim 10^{13} - 10^{14}$ G (e.g., Dotani et al. 1989; Mony et al. 1991; Greenhill et al. 1993; Cui & Smith 2004). The retrograde disc scenario would eliminate the need for such an unusually strong magnetic field, but the pulsar would necessarily be far from its equilibrium spin period (e.g., Makishima et al. 1988; Dotani et al. 1989; Chakrabarty et al. 1997; Nelson et al. 1997a).

The negative correlation of spin-up rate $\dot{\nu}$ and X-ray flux found in BATSE observations in the 1990s (Chakrabarty et al. 1997; Paul et al. 1997) and in this work is also not consistent with the standard disc accretion model by Ghosh & Lamb (1979b), which predicts higher spin-up rates for higher X-ray luminosities. However, it is consistent with a retrograde disc around the neutron star, taking angular momentum off the pulsar, so that higher spin-down rates for higher X-ray luminosities are expected. However, it remains a chief question how a retrograde

disc could form and remain stable over such a long time period (about 30 years).

On the other hand, positive correlations between spin-up rate $\dot{\nu}$ and X-ray luminosity have also been found during the steady spin-down trend (e.g., Chakrabarty et al. 1997). In addition to these positive correlations, during this spin-down steady trend some spin-up episodes related to bright flares, where the source has reached almost the same luminosity as it had in the 1970s, have taken place (e.g., Chakrabarty et al. 1997; Ferrigno et al. 2007). Again, it is not possible to explain this with accretion from a retrograde disc.

The presence of fast flickering has been interpreted as evidence of accretion discs around neutron stars in general (e.g., Horne 1994) and in particular, for GX 1+4 on the basis of such flickering in the optical light curves (e.g., Braga et al. 1993; Jablonski et al. 1997). Meanwhile, the absence of this flickering when the system is faint has been interpreted as episodic interruptions of the accretion (Jablonski et al. 1997). Furthermore, coherent optical pulsations of two minutes found by Jablonski et al. (1997) in GX 1+4 have also been interpreted as a sign of X-ray reprocessing in an accretion disc (Chester 1979) by several authors (e.g., Chakrabarty & Roche 1997). Moreover, Chakrabarty & Roche (1997) have carried out an optical emission-line diagnostic study of the optical and infrared spectra, which also suggested there is an accretion disc around the neutron star.

According to numerical simulations of mass accretion onto the neutron star in wind-fed systems, the accreted specific

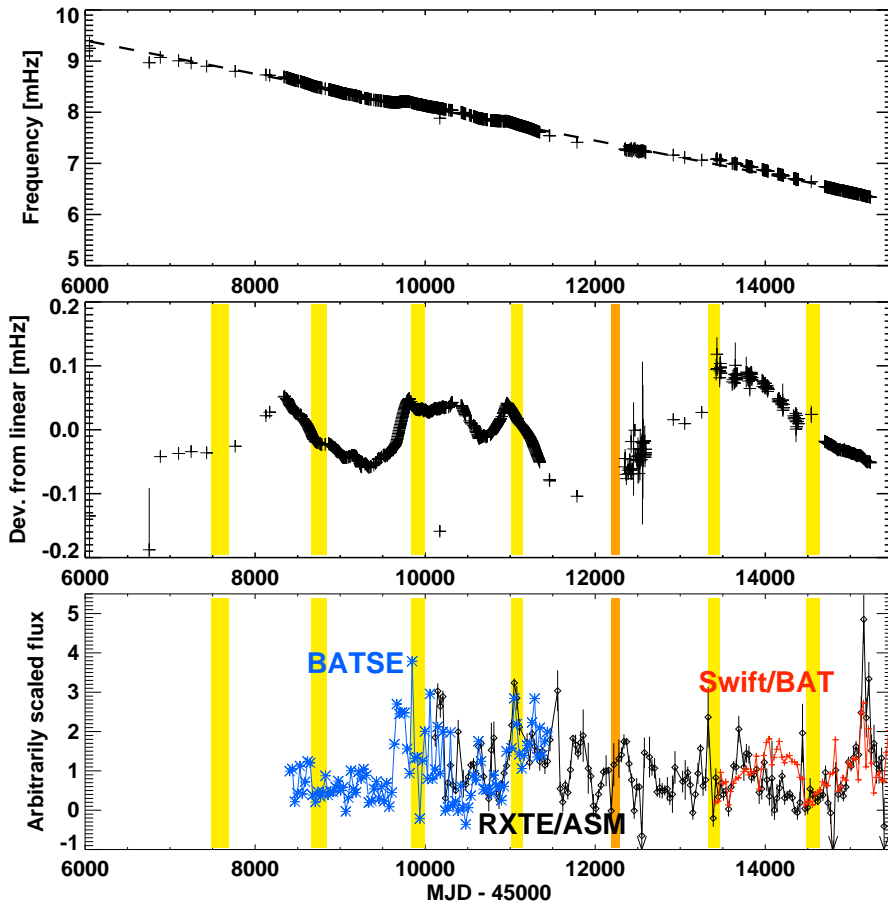


Fig. 7. *Top:* Long-term spin-down of GX 1+4 expressed in frequencies. *Middle:* Residuals from the linear fit to the frequencies. The orange shaded area indicates the perigee passage time, including uncertainties, given by Hinkle et al. (2006). Yellow shaded areas indicate the perigee passage intervals extrapolated from this ephemeris. *Bottom:* Observed X-ray fluxes in arbitrary scaling to the same mean by BATSE, RXTE/ASM, and Swift/BAT, averaged over 30-day intervals.

angular momentum could change sign in an erratic manner, which may lead to alternating spin-up and spin-down episodes (e.g., Taam & Fryxell 1988; Matsuda et al. 1991; Foglizzo et al. 2005). This phenomena, known as “flip-flop”, has been used to explain the random walk of the spin period of sources like Vela X-1 (e.g., Boynton et al. 1984). However, it is important to note that these simulations apply to supergiant stars with powerful winds (see e.g. Kudritzki & Puls 2000), and not to M-giant stars.⁴

Last but not least, the X-ray luminosity increase accompanied by a rather constant spin-down rate observed by, e.g., Ginga in 1987 (Sakao et al. 1990) implies (temporary) luminosity-independent spin-down behaviour. This cannot be understood in terms of either the prograde disc, or the retrograde one.

To conclude, ever since GX 1+4 entered the low-luminosity state around 1984, overall it kept spinning down with the general spin-down accompanied by spin-up episodes during flares. The presence of both positive and negative correlations between X-ray flux and spin-down rate, and episodes of no correlations between X-ray flux and spin-down rate, are not possible to explain either with standard disc accretion or with a retrograde disc. One cannot explain the long-term steady spin-down with an alternating disc either, because the neutron star tends to spin-down (except for short episodes). It can also not be explained by a retrograde

disc, as the spin-down rate is increasing with time while the average X-ray luminosity⁵ is stable around $L_X \sim 10^{35} - 10^{36}$ erg s⁻¹.

5.2. Quasi-spherical accretion in GX 1+4

In this section we discuss how the long-term spin-down behaviour of GX 1+4 presented in Fig. 6 can be explained by quasi-spherical accretion onto the neutron star from the stellar wind from the secondary companion.

In wind-fed pulsars with long orbital periods, accretion onto the neutron star can proceed quasi-spherically; i.e. an accretion disc around the neutron star magnetosphere cannot be formed at all. The formation of the disc depends on whether the specific angular momentum of matter j_m near the magnetospheric radius R_m is larger or smaller than the Keplerian value $j_K(R_m) = \sqrt{GM}R_m$. Assuming the specific angular momentum conservation, j_m can be related to that of gravitationally captured stellar wind matter in the zone of bow shock at the Bondi radius $R_G = 2GM/(V_w^2 + V_{orb}^2) \sim 10^{12}v_7^{-2}$ cm (here v_7 is the relative stellar wind velocity in units of 100 km/s), $j_m = j_w$. To within a numerical factor of order one, $j_w = (2\pi/P_{orb})R_G^2 \approx 3 \times 10^{17}(P_{orb}/1000^d)^{-1}v_7^{-4}$, which can be smaller than $j_K(R_m)$ for typical magnetospheric radii⁶ $R_m = 10^9$ cm, so the formation of quasi-spherical accretion flow is very likely.

⁵ The luminosity value has been corrected to the distance of 4.3 kpc (Hinkle et al. 2006), as are the luminosity values used hereafter.

⁶ The value of the magnetospheric radius is determined by the pressure balance at the magnetospheric boundary, and generally can be notably different for disc and spherical accretion

⁴ V2116 Oph is an M6-giant (Chakrabarty & Roche 1997; Hinkle et al. 2006). Such stars have slow and strongly variable stellar winds (see e.g., Crowley 2006).

There can be two very different regimes. If the X-ray luminosity of the central source is high enough ($\sim 10^{37}$ erg/s), the Compton cooling of plasma in the region of the bow shock is rapid, so the matter freely (supersonically) falls toward the magnetosphere, near which the shock is formed. This regime with different degrees of physical description was considered, e.g., in papers by Arons & Lea (1976), Burnard et al. (1983), Bisnovatyi-Kogan (1991), or Illarionov & Kompaneets (1990). In contrast, the cooling can be ineffective for moderate and low X-ray luminosities, and the matter moves toward the neutron star magnetosphere subsonically, by forming a hot quasi-static shell around the magnetosphere (the settling accretion). Such shells were considered by Davies & Pringle (1980). A superadiabatic temperature gradient can be established in the shell, leading to development of large-scale convective motions and turbulent cascades. Recently, this regime of accretion has been studied by Shakura et al. (in press) (see also first results in Postnov et al. 2010). In the settling accretion regime, the accretion rate onto the neutron star is determined by the ability of plasma to enter the magnetosphere via instabilities, and this determines the mean radial velocity of matter in the shell by the mass conservation law. In the last paper it was found that the critical X-ray luminosity below which the settling accretion regime sets in is about 4×10^{36} erg/s.

In the free-fall accretion regime, the neutron star spin behaviour is determined by the sign of the specific angular momentum of captured matter (prograde or retrograde). Nevertheless, in the case of GX 1+4, this regime seems to be unlikely for two reasons: (a) the X-ray luminosity of the source at the spin-down stage is quite low and (b) the long-term spin-down with short episodic spin-ups are difficult to reconcile with expected features of wind accretion – although alternation of the prograde/retrograde angular momentum of the captured matter in inhomogeneous stellar wind is possible, the predominance of the retrograde sign is very enigmatic.

In contrast, in the settling accretion regime, the hot convective shell can mediate the angular momentum transfer to/from the neutron star magnetosphere, and the neutron star can spin up or down depending on the sign of the difference of angular velocity of matter near the magnetospheric boundary and that of the magnetosphere itself. The gas-dynamic problem of spherically-symmetric accretion flow with cooling and heating due to turbulence (generally, anisotropic) was considered in Shakura et al. (2011). It was found that in this regime with increasing X-ray luminosity, the neutron star spin-down can change for spin-up (even abruptly, if L_x exceeds the critical value for the existence of the shell) and vice versa, and the fluctuations in the spin frequency can anti-correlate with flux fluctuations, which indeed follows from the analysis of BATSE and Fermi/GBM observations of GX 1+4 (see above).

It therefore seems very likely that the settling accretion is under way at the present low-luminosity spin-down state of GX 1+4. Then the source must have had higher X-ray luminosities in the preceding long-term spin-up state. Indeed, at high X-ray luminosities, the Compton cooling near the magnetosphere is very strong and a free-fall gap in the matter flow appears above the magnetosphere, the casual connection between the magnetosphere and the shell is lost, and only spin-up of neutron star is possible.

The fluxes reported during the long-term spin-up phase prior to the 1980s and the luminosities derived from these are generally a few times higher than those reported during the still ongoing spin-down phase. Accounting for the differences in instrumentation and energy ranges and the corresponding uncertainties, we

arrive at luminosities $L_{2-60 \text{ keV}} \sim 1-5 \times 10^{37}$ erg s^{-1} for the early data (e.g., Doty et al. 1981). After the torque reversal, luminosities in this energy interval mostly remain in the range of a few times 10^{36} erg s^{-1} . A flare seen by BATSE (Chakrabarty et al. 1997) had a pulsed flux corresponding to $L_{2-60 \text{ keV}} \sim 9 \times 10^{36}$ erg s^{-1} , which indicates a comparable brightness to the early data. We refer to Appendix A for a more detailed discussion.

The middle panel of Fig. 7 shows long-term quasi-periodic frequency fluctuations. Their fractional amplitude $\Delta\omega/|\omega_{\text{sd}}| = (\delta\dot{\omega}\Delta T) \approx \pm 0.1$ over a time interval of about one orbital period ($\Delta t \approx 1.5 \times 10^8$ s) corresponds to the fractional derivative ratio $\delta\dot{\omega}/|\dot{\omega}_{\text{sd}}| \approx 0.3$. Apparently, they are marginally correlated with periastron passages of the binary system, but not clearly correlated with the X-ray flux variations indicated in the bottom panel of Fig. 7. These long-term fluctuations can be due to smooth variations of the wind density ρ_w and velocity near the gravitational capture radius.

The short-term spin-up episodes sometimes observed on top of a steady spin-down behaviour (see Fig. 2 in Chakrabarty et al. 1997, and Fig. 1 of this paper) are correlated with an enhancement of the X-ray flux, in contrast to the negative frequency-flux correlation at the spin-down discussed above (see Figs. 4 and 5). During these short spin-ups, $\dot{\omega}$ was about half of the average $\dot{\omega}_{\text{su}}$ observed during the steady spin-up state of GX 1+4. The X-ray luminosity during these episodic spin-ups was approximately five times higher than the mean X-ray luminosity during the steady spin-down. These facts are consistent with the quasi-spherical accretion model that predicts transitions from spin-down to spin-up with increasing mean accretion rate and the reversal of flux-period correlation properties (see Shakura et al. 2011 for more detail). However, an increase in the accretion rate by more than one order of magnitude in GX 1+4 could destroy the shell due to rapid radiation cooling and the establishing of the free-fall accretion regime onto the magnetosphere. In that case only spin-up of neutron star is possible.

6. Conclusions

We present the results of observing the pulse period behaviour of the symbiotic X-ray binary GX 1+4. New measurements by BeppoSAX, INTEGRAL, and Fermi confirm the continuing overall spin-down (about ~ 3.4 s/y) of the neutron star since the torque reversal in the early 1980s. The pulse period has increased by about $\sim 50\%$ over the past three decades and has reached the highest value ever observed for this source. The X-ray luminosity during the extended spin-down phase has in general been significantly lower than during the spin-up phase of the 1970s (see Appendix A).

The global spin-down follows a linear trend in angular frequency with deviations $< 2\%$ (see Fig. 7). During this time interval, there have only been brief instances of spin-up observed by BATSE (Chakrabarty et al. 1997) related to bright flares where the X-ray luminosity has almost reached the value it had in the 1970s, and a possible spin-up in 2004 observed by INTEGRAL (Ferrigno et al. 2007).

On top of the long-term spin-up and spin-down trends going on for decades or more independently of the X-ray luminosity, there are pulse period fluctuations on shorter timescales that do show anti-correlation with the source X-ray flux as demonstrated in Section 4 and, apparently, marginally correlated with the orbital phase.

As shown in Secs 5.1 and 5.2, these observational facts are difficult to reconcile with prograde or retrograde disc accretion but can be explained by assuming quasi-spherical accretion onto the

neutron star from the stellar wind of the M-type giant companion.

Acknowledgments. Partially based on observations with INTEGRAL, an ESA project with instruments and a science data centre funded by ESA member states (especially the PI countries: Denmark, France, Germany, Italy, Switzerland, Spain), Czech Republic, and Poland, and with the participation of Russia and the USA. We acknowledge support from the Faculty of the European Space Astronomy Centre (ESAC). The Swift/BAT transient monitor results are provided by the Swift/BAT team. We thank Depto Chakrabarty for providing most of the historical pulse measurements and Jean in't Zand for providing the BeppoSAX/WFC light curves. The work of KP and AK was partially supported by RFBF grant 10-02-00599. M.F. acknowledges partial support from NASA grants NNX08AW06G and NNX11AE24G. The work of AG has been supported by the Spanish MICINN under FPI Fellowship BES-2009-014217 associated to grant AYA2008-06166-C03-03, and partially funded by grants AYA2010-21697-C05-05 and CSD2006-00070 of the Spanish MICINN.

References

- Arons, J. & Lea, S. M. 1976, *ApJ*, 210, 792
- Barthelmy, S. D., Barbier, L. M., Cummings, J. R., et al. 2005, *Space Science Reviews*, 120, 143
- Becker, R. H., Boldt, E. A., Holt, S. S., et al. 1976, *ApJ*, 207, L167
- Bisnovatyi-Kogan, G. S. 1991, *A&A*, 245, 528
- Boella, G., Butler, R. C., Perola, G. C., et al. 1997, *A&AS*, 122, 299
- Boynton, P. E., Deeter, J. E., Lamb, F. K., et al. 1984, *ApJ*, 283, L53
- Braga, J., Jablonski, F. F., Elizalde, F., & Steiner, J. E. 1993, *Rev. Mexicana Astron. Astrofis.*, 26, 113
- Braga, J., Pereira, M. G., & Jablonski, F. J. 2000, in *American Institute of Physics Conference Series*, ed. M. L. McConnell & J. M. Ryan, Vol. 510, 188–192
- Burnard, D. J., Arons, J., & Lea, S. M. 1983, *ApJ*, 266, 175
- Chakrabarty, D., Bildsten, L., Finger, M. H., et al. 1997, *ApJ*, 481, L101
- Chakrabarty, D. & Roche, P. 1997, *ApJ*, 489, 254
- Chester, T. J. 1979, *ApJ*, 227, 569
- Coe, M. J., Engel, A. R., Evans, A. J., & Quenby, J. J. 1981, *ApJ*, 243, 155
- Corbet, R. H. D., Sokolowski, J. L., Mukai, K., Markwardt, C. B., & Tueller, J. 2008, *ApJ*, 675, 1424
- Courvoisier, T., Walter, R., Beckmann, V., et al. 2003, *A&A*, 411, L53
- Crowley, C. 2006, PhD thesis, School of Physics, Trinity College Dublin, Ireland
- Cui, W. & Smith, B. 2004, *ApJ*, 602, 320
- Cutler, E. P., Dennis, B. R., & Dolan, J. F. 1986, *ApJ*, 300, 551
- Damle, S. V., Kunte, P. K., Naranan, S., Sreekantan, B. V., & Leahy, D. A. 1988, *Advances in Space Research*, 8, 415
- David, P., Laurent, P., Denis, M., et al. 1998, *A&A*, 332, 165
- Davidsen, A., Malina, R., & Bowyer, S. 1977, *ApJ*, 211, 866
- Davies, R. E. & Pringle, J. E. 1980, *MNRAS*, 191, 599
- Denis, M., Barret, D., Jourdain, E., et al. 1991, in *International Cosmic Ray Conference*, Vol. 1, International Cosmic Ray Conference, 161–
- Dotani, T., Kii, T., Nagase, F., et al. 1989, *PASJ*, 41, 427
- Doty, J. P., Lewin, W. H. G., & Hoffman, J. A. 1981, *ApJ*, 243, 257
- Edelson, R. A. & Krolik, J. H. 1988, *ApJ*, 333, 646
- Elsner, R. F., Weisskopf, M. C., Apparao, K. M. V., et al. 1985, *ApJ*, 297, 288
- Ferrigno, C., Segreto, A., Santangelo, A., et al. 2007, *A&A*, 462, 995
- Finger, M. H., Bildsten, L., Chakrabarty, D., et al. 1999, *ApJ*, 517, 449
- Fishman, G. J., Meegan, C. A., Wilson, R. B., Paciesas, W. S., & Pendleton, G. N. 1992, in *NASA Conference Publication*, ed. C. R. Shrader, N. Gehrels, & B. Dennis, Vol. 3137, 26–34
- Foglizzo, T., Galletti, P., & Ruffert, M. 2005, *A&A*, 435, 397
- Gehrels, N., Chincarini, G., Giommi, P., et al. 2004, *ApJ*, 611, 1005
- Gehrels, N., Chipman, E., & Kniffen, D. A. 1993, *A&AS*, 97, 5
- Ghosh, P. & Lamb, F. K. 1977, in *Bulletin of the American Astronomical Society*, Vol. 9, 631
- Ghosh, P. & Lamb, F. K. 1979a, *ApJ*, 232, 259
- Ghosh, P. & Lamb, F. K. 1979b, *ApJ*, 234, 296
- Giacconi, R., Gursky, H., Kellogg, E., Schreier, E., & Tananbaum, H. 1971, *ApJ*, 167, L67
- Glass, I. S. & Feast, M. W. 1973, *Nature*, 245, 39
- Greenhill, J. G., Sharma, D. P., Dieters, S. W. B., et al. 1993, *MNRAS*, 260, 21
- Hall, R. & Davelaar, J. 1983, *IAU Circ.*, 3872
- Hinkle, K. H., Fekel, F. C., Joyce, R. R., et al. 2006, *ApJ*, 641, 479
- Horne, K. 1994, in *HST Proposal*, 5498
- Illarionov, A. F. & Kompaneets, D. A. 1990, *MNRAS*, 247, 219
- in't Zand, J., Verbunt, F., Heise, J., et al. 2004, *Nuclear Physics B Proceedings Supplements*, 132, 486
- Jablonski, F. J., Pereira, M. G., Braga, J., & Gneiding, C. D. 1997, *ApJ*, 482, L171
- Jager, R., Mels, W. A., Brinkman, A. C., et al. 1997, *A&AS*, 125, 557
- Jayanthi, U. B., Jablonski, F., & Braga, J. 1987, *Ap&SS*, 138, 183
- Kaneko, Y., Preece, R. D., Briggs, M. S., et al. 2006, *ApJS*, 166, 298
- Kendziorra, E., Staubert, R., Reppin, C., et al. 1982, in *Galactic X-ray sources*, ed. P. W. Sanford, P. Laskarides, & J. Salton, 205
- Koo, J.-W. C. & Haymes, R. C. 1980, *ApJ*, 239, L57
- Kotani, T., Dotani, T., Nagase, F., et al. 1999, *ApJ*, 510, 369
- Kudritzki, R. & Puls, J. 2000, *ARA&A*, 38, 613
- Kuulkers, E., Shaw, S. E., Paizis, A., et al. 2007, *A&A*, 466, 595
- Larsson, S. 1996, *A&AS*, 117, 197
- Laurent, P., Salotti, L., Paul, J., et al. 1993, *A&A*, 278, 444
- Leahy, D. A. 1989, in *Bulletin of the American Astronomical Society*, Vol. 21, 749
- Lebrun, F., Leray, J. P., Lavocat, P., et al. 2003, *A&A*, 411, L141
- Lewin, W. H. G., Ricker, G. R., & McClintock, J. E. 1971, *ApJ*, 169, L17
- Lovelace, R. V. E., Romanova, M. M., & Bisnovatyi-Kogan, G. S. 1995, *MNRAS*, 275, 244
- Lutovinov, A. A., Grebenev, S. A., Syunyaev, R. A., & Pavlinskii, M. N. 1994, *Astronomy Letters*, 20, 538
- Makishima, K., Ohashi, T., Sakao, T., et al. 1988, *Nature*, 333, 746
- Mandrou, P., Roques, J. P., Bouchet, L., et al. 1994, *ApJS*, 92, 343
- Markert, T. H., Laird, F. N., Clark, G. W., et al. 1979, *ApJS*, 39, 573
- Masetti, N., Landi, R., Pretorius, M. L., et al. 2007, *A&A*, 470, 331
- Masetti, N., Orlandini, M., Palazzi, E., Amati, L., & Frontera, F. 2006, *A&A*, 453, 295
- Matsuda, T., Sekino, N., Sawada, K., et al. 1991, *A&A*, 248, 301
- McClintock, J. E. & Leventhal, M. 1989, *ApJ*, 346, 143
- Meegan, C., Lichti, G., Bhat, P. N., et al. 2009, *ApJ*, 702, 791
- Mony, B., Kendziorra, E., Maisack, M., et al. 1991, *A&A*, 247, 405
- Mukai, K. 1988, *MSSL internal report*
- Nagase, F. 1989, *PASJ*, 41, 1
- Naik, S., Paul, B., & Callanan, P. J. 2005, *ApJ*, 618, 866
- Nelson, R. W., Bildsten, L., Chakrabarty, D., et al. 1997a, *ApJ*, 488, L117
- Nelson, R. W., Vaughan, B. A., Bildsten, L., et al. 1997b, in *Astronomical Society of the Pacific Conference Series*, Vol. 121, IAU Colloq. 163: *Accretion Phenomena and Related Outflows*, ed. D. T. Wickramasinghe, G. V. Bicknell, & L. Ferrario, 256
- Paul, B., Dotani, T., Nagase, F., Mukherjee, U., & Naik, S. 2005, *ApJ*, 627, 915
- Paul, B., Rao, A. R., & Singh, K. P. 1997, *A&A*, 320, L9
- Pereira, M. G., Braga, J., & Jablonski, F. 1999, *ApJ*, 526, L105
- Peterson, B. M., Wanders, I., Horne, K., et al. 1998, *PASP*, 110, 660
- Postnov, K., Shakura, N., González-Galán, A., et al. 2010, in *Proceedings of the 8th INTEGRAL Workshop*
- Predehl, P., Friedrich, S., & Staubert, R. 1995, *A&A*, 294, L33
- Rea, N., Stella, L., Israel, G. L., et al. 2005, *MNRAS*, 364, 1229
- Ricketts, M. J., Hall, R., Page, C. G., Whitford, C. H., & Pounds, K. A. 1982, *MNRAS*, 201, 759
- Ritz, S. M., Gehrels, N., McEnery, J. E., et al. 2009, in *Bulletin of the American Astronomical Society*, Vol. 41, 416
- Sakao, T., Kohmura, Y., Makishima, K., et al. 1990, *MNRAS*, 246, 11P
- Shahbaz, T., Smale, A. P., Naylor, T., et al. 1996, *MNRAS*, 282, 1437
- Shakura, N., Postnov, K., Kochetkova, A., & Hjalmarsdotter, L. in press, *MNRAS*
- Strickman, M. S., Johnson, W. N., & Kurfess, J. D. 1980, *ApJ*, 240, L21
- Taam, R. E. & Fryxell, B. A. 1988, in *Bulletin of the American Astronomical Society*, Vol. 20, 1043
- Tananbaum, H., Gursky, H., Kellogg, E. M., et al. 1972, *ApJ*, 174, L143
- The, P. S., Thomas, D., Christensen, C. G., & Westerlund, B. E. 1990, *PASP*, 102, 565
- Ubertini, P., Lebrun, F., Di Cocco, G., et al. 2003, *A&A*, 411, L131
- Wang, Y. 1987, *A&A*, 183, 257
- Warwick, R. S., Marshall, N., Fraser, G. W., et al. 1981, *MNRAS*, 197, 865
- White, N. E., Mason, K. O., Huckle, H. E., Charles, P. A., & Sanford, P. W. 1976, *ApJ*, 209, L119
- White, N. E., Swank, J. H., & Holt, S. S. 1983, *ApJ*, 270, 711
- Winkler, C., Courvoisier, T., Di Cocco, G., et al. 2003, *A&A*, 411, L1

Appendix A: Historical spin period and X-ray flux evolution of GX 1+4

In this section we attempt to summarize the evolution of the spin period, as well as of the brightness of GX 1+4. For a table of all pulse period measurements, we refer to Appendix B. The former is rather straightforward, the latter much less so. The difficulty arises for various reasons. First of all, the flux values come from a variety of instruments with different energy ranges and spectral responses. Second, few publications give enough detail to determine the exact spectral shape used in the analysis. Finally, different broad-band observations (e.g., Naik et al. 2005) do demonstrate clear spectral variation, including a variable absorption.

To get a basis for comparison of flux we used the detailed spectral shapes published by Naik et al. (2005) and Ferrigno et al. (2007) to simulate a range of spectra under different conditions. We varied crucial spectral parameters within the uncertainties given for these spectra to cover more of the possible parameter range. From these simulated spectra we then derived simulated fluxes in various energy ranges and used the ratio of these fluxes to derive flux conversion factors between the bands, together with the corresponding uncertainties. Based on this analysis, we converted selected fluxes to the 2–60 keV band, for which fluxes were reported by Cui & Smith (2004) and Ferrigno et al. (2007) and very close to the SAS 3 band (1.2–55 keV) for which fluxes are reported in Doty et al. (1981).

The uncertainty in such conversions can be fairly high, especially when going from a narrow band to a broader band. In our analysis we estimate these to be up to, e.g., ~55% scaling a 2–6 keV flux to the 2–60 keV band, while allowing for uncertainties in the soft band spectral shape and the level of absorption at any given time. Therefore, we concentrate as much as possible on fluxes that can be compared directly for our discussion.

For an earlier overview of the flux evolution of GX 1+4 between 1970 and 1988 we refer to Table 2 of McClintock & Leventhal (1989).

A.1. Early observation – the spin-up phase

After its detection in the 1970s GX 1+4 was spinning up with the fastest rate ($\dot{P} \sim -8.5 \times 10^{-8} \text{ s s}^{-1}$ or -2.55 yr^{-1}) among the known X-ray pulsars at the time (e.g., Doty et al. 1981; Elsner et al. 1985; Nagase 1989). The OSO-7 scans between October 1971 and May 1973 found flux values in the Argon counters varying between ~ 2 and $\sim 12 \text{ cts s}^{-1}$ (Markert et al. 1979), which roughly scales⁷ to a flux in the 2–60 keV band of $(3 \pm 1 - 18 \pm 6) \times 10^{-9} \text{ ergs cm}^{-2} \text{ s}^{-1}$. From SAS3 observations in 1975 and 1976, Doty et al. (1981) found fluxes in the 1.2–55 keV range of $(4.5 \pm 1 - 22 \pm 10) \times 10^{-9} \text{ ergs cm}^{-2} \text{ s}^{-1}$, comparable, within the uncertainties, to OSO-8 observations (Becker et al. 1976).

A.2. Low state and torque reversal

EXOSAT failed to detect the source in 1983 and 1984, revealing an extended low state with upper limits on the 2–10 keV flux of $< 10^{-10} \text{ ergs cm}^{-2} \text{ s}^{-1}$ (Hall & Davelaar 1983) and $< 10^{-11} \text{ ergs cm}^{-2} \text{ s}^{-1}$ (Mukai 1988), respectively. Even allowing for a factor 3–7 when scaling this to the broader energy range above and accounting for various uncertainties, the source was fainter by two orders of magnitude or more during the spin-up phase.

A first detection by Ginga in March 1987 (Makishima et al. 1988; Dotani et al. 1989) found the source still very faint at $\sim 10^{-10} \text{ ergs cm}^{-2} \text{ s}^{-1}$ in the 2–20 keV band (scaling to roughly twice this value in 2–60 keV). The pulse period of $110.223 \pm 0.003 \text{ s}$ was longer than the last previous measurement (Ricketts et al. 1982), demonstrating that a torque reversal had taken place and the source was spinning down (see Fig. 6 and Table B.1). In addition, the pulse profile of that early observation was peculiar and very different from previously observed ones.

A.3. Early spin-down phase

HEXE and Ginga observations between 1987 and 1989 (Dotani et al. 1989; Sakao et al. 1990; Mony et al. 1991) revealed a remarkably constant spin-down rate at $\dot{P} \sim 4.5 \times 10^{-8} \text{ s s}^{-1}$ in spite of a further overall increase in the X-ray brightness. Ginga fluxes from March 1988 and August 1989 were reported at five to six times that of the first detection in March 1987 (Sakao et al. 1990). No correlation between spin torque and X-ray flux was reported during this period.

GX 1+4 was observed by GRANAT/SIGMA during 1990 and 1991 (Denis et al. 1991). The spin-down of the pulsar was confirmed, but at a lower rate ($\dot{P} \sim 2.6 \times 10^{-8} \text{ s s}^{-1}$). The linear spin-down trend was recovered around September 1991 with a slightly increased rate over the one observed before 1990 (Mandrou et al. 1994).

Ginga observations in September 1990 and September 1991 showed a decrease in the 2–20 keV X-ray fluxes to ~ 6 and $\sim 2 \times 10^{-10} \text{ ergs cm}^{-2} \text{ s}^{-1}$, respectively, suggesting another low state, together with a drastic increase in N_{H} (Kotani et al. 1999). Despite this, the spin-down rate was found to be very stable at $\dot{P} \sim (3 - 4) \times 10^{-8} \text{ s s}^{-1}$.

A.4. Regular monitoring – spin-down with interruptions

BATSE onboard CGRO monitored GX 1+4 daily between April 1991 and September 1994. The average X-ray flux in the 20–60 keV range was $\sim 2 \times 10^{-10} \text{ ergs cm}^{-2} \text{ s}^{-1}$, but interrupted by intermittent bright flares of about 20 day duration (Chakrabarty et al. 1997). During this time a negative correlation between spin-up torque and X-ray flux, i.e., stronger spin-down for higher flux, was observed (e.g., Paul et al. 1997; Chakrabarty et al. 1997; Nelson et al. 1997a).

⁷ See also <http://www.astronomycafe.net/qadir/q1723.html>

In September 1994 an ASCA observation found the source brighter again with a 2–20 keV flux of $\sim 9 \times 10^{-10}$ ergs cm $^{-2}$ s $^{-1}$ (Kotani et al. 1999). One month later, BATSE detected a ~ 200 day bright state, when the pulsar started to spin-up, resuming the spin-down when the low state was recovered (Chakrabarty et al. 1997).

BATSE observations between May 1995 and June 1996 showed an erratically varying X-ray luminosity, although the pulsar continued to spin-down at a relatively steady rate with a weak negative peak at zero lag in the cross-correlation of torque and flux histories (Chakrabarty et al. 1997). After a period of low activity for about a month, GX 1+4 reappeared briefly in a bright flare, during which it transited to spin-up (Chakrabarty et al. 1997). The *pulsed flux* in this flare was $\sim 2 \times 10^{-9}$ ergs cm $^{-2}$ s $^{-1}$ in the 20–60 keV band. According to our analysis, this would correspond to a $\sim (3 - 4.5) \times 10^{-9}$ ergs cm $^{-2}$ s $^{-1}$ *pulsed flux* in the 2–60 keV broad band.

About ten days after this flare, the source dropped below the detection limit and remained undetected until December 1996. During this low state, a series of RXTE observations also failed to detect GX 1+4, giving an upper limit for the X-ray luminosity that was comparable to the 1983/1984 EXOSAT low state (Chakrabarty et al. 1997).

Cui & Smith (2004) monitored GX 1+4 weekly with RXTE in 2001 and 2002. While the source was “quite bright” at the beginning of the year 2002 with fluxes (2–60 keV) of $\sim (2 - 3) \times 10^{-9}$ ergs cm $^{-2}$ s $^{-1}$, it made a transition to a faint state in mid June, reaching a minimum flux of $\sim 3 \times 10^{-11}$ ergs cm $^{-2}$ s $^{-1}$, again comparable to the EXOSAT upper limits during the time of the torque reversal. At fluxes below $\sim 2 \times 10^{-10}$ ergs cm $^{-2}$ s $^{-1}$ some observations had no detectable X-ray pulsations, while others presented a clearly pulsed signal. Towards the end of the year, the X-ray luminosity increased again. A joint Chandra & RXTE observation in August 2002 found a 2–20 keV X-ray flux of 3.8×10^{-11} ergs cm $^{-2}$ s $^{-1}$ (Paul et al. 2005). The average spin-down rate during this period was $\dot{P} \sim 4.4 \times 10^{-8}$ s s $^{-1}$ (Cui & Smith 2004).

During INTEGRAL observations between March 2003 and September 2004 (Ferrigno et al. 2007) the source increased its flux by about a factor of 5, with erratic variations of about one order of magnitude. For two time periods with broad-band coverage by the INTEGRAL instruments in February/March and September 2004, Ferrigno et al. (2007) determined the 2–60 fluxes to be $\sim 1.7 \times 10^{-9}$ ergs cm $^{-2}$ s $^{-1}$ and $\sim 2.3 \times 10^{-9}$ ergs cm $^{-2}$ s $^{-1}$, respectively.

The secular spin-down trend of GX 1+4 at the time was $\dot{P} \sim 6.6 \times 10^{-8}$ s/s, with a spin-up of the source observed during the high-luminosity state in September 2004 (Ferrigno et al. 2007).

For more recent data we refer to Secs 2 and 4.

Appendix B: GX 1+4 pulse period measurements

For reference we have collected all pulse period measurements presented in Fig. 6 and give them in Table B.1 below.

Table B.1. Pulse period measurements of GX 1+4

MJD	$P_{spin}(s)$	Instrument	MJD	$P_{spin}(s)$	Instrument
40875.5	135.0 ± 4.0	MIT balloon ¹	41571.5	129.0 ± 0.3	Copernicus ²
41578.5	129.6 ± 0.6	Copernicus ²	41766.5	131.7 ± 4.2	Copernicus ²
42139.5	128.1 ± 0.3	Rice balloon ³	42670.5	122.46 ± 0.03	OSO-8 ⁴
42695.2	122.34 ± 0.06	SAS-3 ⁵	42772.8	121.367 ± 0.004	SAS-3 ⁵
42812.1	120.6589 ± 0.0003	SAS-3 ⁵	42853.5	120.493 ± 0.003	OSO-8 ⁶
42909.3	120.5 ± 0.5	NRL balloon ⁷	42963.2	120.19 ± 0.05	SAS-3 ⁵
43213.5	118.873 ± 0.005	OSO-8 ⁶	43244.5	118.715 ± 0.005	Ariel 5 ⁸
43470.6	117.45 ± 0.20	NRL balloon ⁷	43593.5	116.49 ± 0.10	OSO-8 ⁶
43772.0	114.254 ± 0.011	OSO-8 ⁶	43834.5	113.75 ± 0.25	MPI/Tuebingen balloon ⁹
43952.5	112.68 ± 0.03	Einstein/MPC ¹⁰	44062.95	112.076 ± 0.003	Ariel 6 ¹¹
44346.95	109.668 ± 0.003	Ariel 6 ¹¹	45060.0	108.8 ± 0.2	Balloon experiment ¹²
46052.0	108.1 ± 2.6	TIFR balloon ^{13, 14}	46754.25	111.5 ± 1.2	Tasmania balloon ¹⁵
46885.0	110.233 ± 0.003	Ginga ¹⁶	47099.54	111.03 ± 0.02	Mir/Kvant/HEXE ¹⁷
47247.3	111.59 ± 0.02	Ginga ¹⁸	47429.61	112.359 ± 0.005	Mir/Kvant/HEXE ¹⁷
47765.47	113.626 ± 0.002	Ginga ¹⁹	48126.8	114.540 ± 0.062	GRANAT/ART-P ²⁰
48171.7	114.657 ± 0.014	GRANAT/ART-P ²⁰	48337.87	115.06 ± 0.03	GRANAT/SIGMA ²¹
48347.52	115.086 ± 0.005	GRANAT/SIGMA ²¹	48368.5	115.2280 ± 0.0016	CGRO/BATSE ²²
48373.5	115.2617 ± 0.0022	CGRO/BATSE ²²	48378.5	115.2932 ± 0.0025	CGRO/BATSE ²²
48383.5	115.3301 ± 0.0016	CGRO/BATSE ²²	48388.5	115.3664 ± 0.0016	CGRO/BATSE ²²
48393.5	115.4112 ± 0.0014	CGRO/BATSE ²²	48398.5	115.4567 ± 0.0015	CGRO/BATSE ²²
48403.5	115.5001 ± 0.0013	CGRO/BATSE ²²	48408.5	115.5352 ± 0.0013	CGRO/BATSE ²²
48413.5	115.5668 ± 0.0017	CGRO/BATSE ²²	48418.5	115.5978 ± 0.0025	CGRO/BATSE ²²
48423.5	115.6323 ± 0.0021	CGRO/BATSE ²²	48428.5	115.6617 ± 0.0018	CGRO/BATSE ²²
48433.5	115.7029 ± 0.0021	CGRO/BATSE ²²	48438.5	115.7378 ± 0.0017	CGRO/BATSE ²²
48443.5	115.7689 ± 0.0020	CGRO/BATSE ²²	48448.5	115.8091 ± 0.0023	CGRO/BATSE ²²
48453.5	115.8482 ± 0.0017	CGRO/BATSE ²²	48458.5	115.8836 ± 0.0020	CGRO/BATSE ²²
48463.5	115.9148 ± 0.0025	CGRO/BATSE ²²	48468.5	115.9493 ± 0.0018	CGRO/BATSE ²²
48473.5	115.9780 ± 0.0024	CGRO/BATSE ²²	48478.5	116.0134 ± 0.0023	CGRO/BATSE ²²
48483.5	116.0383 ± 0.0061	CGRO/BATSE ²²	48488.5	116.0648 ± 0.0052	CGRO/BATSE ²²
48493.5	116.0820 ± 0.0038	CGRO/BATSE ²²	48498.5	116.1130 ± 0.0031	CGRO/BATSE ²²
48503.5	116.1392 ± 0.0040	CGRO/BATSE ²²	48508.5	116.1592 ± 0.0027	CGRO/BATSE ²²
48513.5	116.1799 ± 0.0022	CGRO/BATSE ²²	48533.5	116.3084 ± 0.0044	CGRO/BATSE ²²
48538.5	116.3213 ± 0.0028	CGRO/BATSE ²²	48543.5	116.3713 ± 0.0014	CGRO/BATSE ²²
48548.5	116.4208 ± 0.0014	CGRO/BATSE ²²	48553.5	116.4638 ± 0.0040	CGRO/BATSE ²²
48558.5	116.4749 ± 0.0052	CGRO/BATSE ²²	48563.5	116.5092 ± 0.0029	CGRO/BATSE ²²
48568.5	116.5421 ± 0.0034	CGRO/BATSE ²²	48573.5	116.5774 ± 0.0014	CGRO/BATSE ²²
48578.5	116.6152 ± 0.0017	CGRO/BATSE ²²	48583.5	116.6493 ± 0.0019	CGRO/BATSE ²²
48588.5	116.6926 ± 0.0041	CGRO/BATSE ²²	48593.5	116.7240 ± 0.0028	CGRO/BATSE ²²
48598.5	116.7618 ± 0.0025	CGRO/BATSE ²²	48603.5	116.7910 ± 0.0019	CGRO/BATSE ²²
48608.5	116.8300 ± 0.0020	CGRO/BATSE ²²	48613.5	116.8659 ± 0.0020	CGRO/BATSE ²²
48618.5	116.9093 ± 0.0016	CGRO/BATSE ²²	48623.5	116.9486 ± 0.0017	CGRO/BATSE ²²
48628.5	116.9918 ± 0.0014	CGRO/BATSE ²²	48633.5	117.0330 ± 0.0012	CGRO/BATSE ²²
48638.5	117.0752 ± 0.0013	CGRO/BATSE ²²	48643.5	117.1177 ± 0.0014	CGRO/BATSE ²²
48648.5	117.1563 ± 0.0017	CGRO/BATSE ²²	48653.5	117.2024 ± 0.0019	CGRO/BATSE ²²
48658.5	117.2400 ± 0.0020	CGRO/BATSE ²²	48663.5	117.2894 ± 0.0014	CGRO/BATSE ²²
48668.5	117.3327 ± 0.0011	CGRO/BATSE ²²	48671.0	117.3590 ± 0.0160	GRANAT/SIGMA ²³
48673.5	117.3786 ± 0.0013	CGRO/BATSE ²²	48678.5	117.4225 ± 0.0014	CGRO/BATSE ²²
48683.5	117.4645 ± 0.0015	CGRO/BATSE ²²	48688.5	117.4987 ± 0.0030	CGRO/BATSE ²²
48693.5	117.5280 ± 0.0053	CGRO/BATSE ²²	48703.5	117.6059 ± 0.0027	CGRO/BATSE ²²
48708.5	117.6299 ± 0.0041	CGRO/BATSE ²²	48713.5	117.6581 ± 0.0036	CGRO/BATSE ²²
48718.5	117.6943 ± 0.0024	CGRO/BATSE ²²	48723.5	117.7281 ± 0.0034	CGRO/BATSE ²²
48728.5	117.7519 ± 0.0040	CGRO/BATSE ²²	48733.5	117.7791 ± 0.0041	CGRO/BATSE ²²
48738.5	117.8007 ± 0.0045	CGRO/BATSE ²²	48743.5	117.8245 ± 0.0059	CGRO/BATSE ²²
48748.5	117.8547 ± 0.0026	CGRO/BATSE ²²	48758.5	117.9050 ± 0.0038	CGRO/BATSE ²²
48763.5	117.9317 ± 0.0029	CGRO/BATSE ²²	48768.5	117.9654 ± 0.0020	CGRO/BATSE ²²
48773.5	117.9887 ± 0.0024	CGRO/BATSE ²²	48778.5	118.0121 ± 0.0043	CGRO/BATSE ²²
48788.5	118.0692 ± 0.0045	CGRO/BATSE ²²	48793.5	118.0842 ± 0.0048	CGRO/BATSE ²²
48808.5	118.1588 ± 0.0053	CGRO/BATSE ²²	48813.5	118.1920 ± 0.0067	CGRO/BATSE ²²
48818.5	118.2127 ± 0.0047	CGRO/BATSE ²²	48823.5	118.2317 ± 0.0042	CGRO/BATSE ²²
48828.5	118.2550 ± 0.0061	CGRO/BATSE ²²	48833.5	118.2585 ± 0.0083	CGRO/BATSE ²²
48838.5	118.2925 ± 0.0050	CGRO/BATSE ²²	48843.5	118.3115 ± 0.0042	CGRO/BATSE ²²

Table B.1. Pulse period measurements of GX 1+4 (continued).

MJD	P_{spin} (s)	Instrument	MJD	P_{spin} (s)	Instrument
48848.5	118.3342 ± 0.0056	CGRO/BATSE ²²	48858.5	118.3761 ± 0.0037	CGRO/BATSE ²²
48863.5	118.4001 ± 0.0072	CGRO/BATSE ²²	48868.5	118.4083 ± 0.0043	CGRO/BATSE ²²
48873.5	118.4485 ± 0.0025	CGRO/BATSE ²²	48878.5	118.4775 ± 0.0050	CGRO/BATSE ²²
48883.5	118.5092 ± 0.0072	CGRO/BATSE ²²	48888.5	118.5331 ± 0.0045	CGRO/BATSE ²²
48893.5	118.5587 ± 0.0033	CGRO/BATSE ²²	48898.5	118.5938 ± 0.0024	CGRO/BATSE ²²
48903.5	118.6269 ± 0.0021	CGRO/BATSE ²²	48908.5	118.6541 ± 0.0024	CGRO/BATSE ²²
48913.5	118.6938 ± 0.0024	CGRO/BATSE ²²	48918.5	118.7237 ± 0.0023	CGRO/BATSE ²²
48923.5	118.7449 ± 0.0040	CGRO/BATSE ²²	48928.5	118.7706 ± 0.0037	CGRO/BATSE ²²
48933.5	118.7982 ± 0.0022	CGRO/BATSE ²²	48938.5	118.8347 ± 0.0020	CGRO/BATSE ²²
48943.5	118.8681 ± 0.0020	CGRO/BATSE ²²	48948.5	118.9047 ± 0.0020	CGRO/BATSE ²²
48953.5	118.9359 ± 0.0027	CGRO/BATSE ²²	48958.5	118.9641 ± 0.0045	CGRO/BATSE ²²
48963.5	119.0017 ± 0.0026	CGRO/BATSE ²²	48968.5	119.0269 ± 0.0038	CGRO/BATSE ²²
48973.5	119.0432 ± 0.0039	CGRO/BATSE ²²	48978.5	119.0783 ± 0.0029	CGRO/BATSE ²²
48983.5	119.1106 ± 0.0023	CGRO/BATSE ²²	48988.5	119.1483 ± 0.0019	CGRO/BATSE ²²
48993.5	119.1940 ± 0.0020	CGRO/BATSE ²²	48998.5	119.2373 ± 0.0019	CGRO/BATSE ²²
49003.5	119.2769 ± 0.0028	CGRO/BATSE ²²	49008.5	119.3053 ± 0.0041	CGRO/BATSE ²²
49013.5	119.3430 ± 0.0039	CGRO/BATSE ²²	49018.5	119.3886 ± 0.0025	CGRO/BATSE ²²
49023.5	119.4221 ± 0.0017	CGRO/BATSE ²²	49028.5	119.4549 ± 0.0019	CGRO/BATSE ²²
49033.5	119.4886 ± 0.0023	CGRO/BATSE ²²	49038.5	119.5085 ± 0.0028	CGRO/BATSE ²²
49043.5	119.5367 ± 0.0044	CGRO/BATSE ²²	49048.5	119.5562 ± 0.0027	CGRO/BATSE ²²
49053.5	119.5777 ± 0.0044	CGRO/BATSE ²²	49058.5	119.5973 ± 0.0041	CGRO/BATSE ²²
49063.5	119.6168 ± 0.0029	CGRO/BATSE ²²	49068.5	119.6441 ± 0.0027	CGRO/BATSE ²²
49073.5	119.6639 ± 0.0030	CGRO/BATSE ²²	49078.5	119.6938 ± 0.0031	CGRO/BATSE ²²
49083.5	119.7111 ± 0.0047	CGRO/BATSE ²²	49088.5	119.7352 ± 0.0044	CGRO/BATSE ²²
49093.5	119.7539 ± 0.0046	CGRO/BATSE ²²	49098.5	119.7773 ± 0.0041	CGRO/BATSE ²²
49103.5	119.7868 ± 0.0078	CGRO/BATSE ²²	49108.5	119.8148 ± 0.0029	CGRO/BATSE ²²
49118.5	119.8550 ± 0.0048	CGRO/BATSE ²²	49123.5	119.8667 ± 0.0059	CGRO/BATSE ²²
49128.5	119.8897 ± 0.0074	CGRO/BATSE ²²	49133.5	119.9099 ± 0.0069	CGRO/BATSE ²²
49138.5	119.9292 ± 0.0039	CGRO/BATSE ²²	49148.5	119.9736 ± 0.0038	CGRO/BATSE ²²
49153.5	119.9993 ± 0.0055	CGRO/BATSE ²²	49158.5	120.0206 ± 0.0035	CGRO/BATSE ²²
49163.5	120.0446 ± 0.0026	CGRO/BATSE ²²	49168.5	120.0767 ± 0.0018	CGRO/BATSE ²²
49173.5	120.1002 ± 0.0014	CGRO/BATSE ²²	49178.5	120.1274 ± 0.0015	CGRO/BATSE ²²
49183.5	120.1575 ± 0.0017	CGRO/BATSE ²²	49188.5	120.1903 ± 0.0018	CGRO/BATSE ²²
49193.5	120.2209 ± 0.0021	CGRO/BATSE ²²	49198.5	120.2545 ± 0.0027	CGRO/BATSE ²²
49203.5	120.3001 ± 0.0042	CGRO/BATSE ²²	49208.5	120.3250 ± 0.0057	CGRO/BATSE ²²
49218.5	120.4089 ± 0.0028	CGRO/BATSE ²²	49223.5	120.4351 ± 0.0026	CGRO/BATSE ²²
49228.5	120.4876 ± 0.0016	CGRO/BATSE ²²	49232.0	120.5560 ± 0.0240	GRANAT/SIGMA ²³
49233.0	120.5570 ± 0.0280	GRANAT/SIGMA ²³	49233.5	120.5371 ± 0.0014	CGRO/BATSE ²²
49236.0	120.5730 ± 0.0150	GRANAT/SIGMA ²³	49238.0	120.5870 ± 0.0150	GRANAT/SIGMA ²³
49238.5	120.5885 ± 0.0016	CGRO/BATSE ²²	49242.0	120.6440 ± 0.0150	GRANAT/SIGMA ²³
49243.5	120.6464 ± 0.0014	CGRO/BATSE ²²	49244.0	120.6680 ± 0.0200	GRANAT/SIGMA ²³
49246.0	120.6750 ± 0.0080	GRANAT/SIGMA ²³	49248.5	120.7016 ± 0.0030	CGRO/BATSE ²²
49249.0	120.7080 ± 0.0160	GRANAT/SIGMA ²³	49253.5	120.7252 ± 0.0043	CGRO/BATSE ²²
49258.5	120.7591 ± 0.0047	CGRO/BATSE ²²	49263.5	120.7738 ± 0.0035	CGRO/BATSE ²²
49268.5	120.8137 ± 0.0052	CGRO/BATSE ²²	49273.5	120.8374 ± 0.0076	CGRO/BATSE ²²
49288.5	120.8429 ± 0.0043	CGRO/BATSE ²²	49293.5	120.8426 ± 0.0033	CGRO/BATSE ²²
49298.5	120.8701 ± 0.0042	CGRO/BATSE ²²	49303.5	120.9023 ± 0.0045	CGRO/BATSE ²²
49308.5	120.9368 ± 0.0032	CGRO/BATSE ²²	49313.5	120.9719 ± 0.0024	CGRO/BATSE ²²
49318.5	121.0084 ± 0.0020	CGRO/BATSE ²²	49323.5	121.0422 ± 0.0019	CGRO/BATSE ²²
49328.5	121.0770 ± 0.0021	CGRO/BATSE ²²	49333.5	121.1123 ± 0.0024	CGRO/BATSE ²²
49338.5	121.1465 ± 0.0021	CGRO/BATSE ²²	49343.5	121.1893 ± 0.0048	CGRO/BATSE ²²
49363.5	121.3394 ± 0.0043	CGRO/BATSE ²²	49368.5	121.3456 ± 0.0072	CGRO/BATSE ²²
49388.5	121.3486 ± 0.0048	CGRO/BATSE ²²	49398.5	121.3689 ± 0.0061	CGRO/BATSE ²²
49403.5	121.3977 ± 0.0083	CGRO/BATSE ²²	49408.5	121.4013 ± 0.0070	CGRO/BATSE ²²
49413.5	121.4083 ± 0.0055	CGRO/BATSE ²²	49418.5	121.4174 ± 0.0045	CGRO/BATSE ²²
49423.5	121.4414 ± 0.0030	CGRO/BATSE ²²	49438.5	121.4471 ± 0.0079	CGRO/BATSE ²²
49443.5	121.4712 ± 0.0033	CGRO/BATSE ²²	49448.5	121.4846 ± 0.0026	CGRO/BATSE ²²
49453.5	121.4922 ± 0.0027	CGRO/BATSE ²²	49458.5	121.5273 ± 0.0055	CGRO/BATSE ²²
49468.5	121.5630 ± 0.0073	CGRO/BATSE ²²	49473.5	121.5816 ± 0.0038	CGRO/BATSE ²²
49478.5	121.6012 ± 0.0033	CGRO/BATSE ²²	49483.5	121.6208 ± 0.0039	CGRO/BATSE ²²
49488.5	121.6330 ± 0.0045	CGRO/BATSE ²²	49493.5	121.6247 ± 0.0074	CGRO/BATSE ²²
49498.5	121.6371 ± 0.0041	CGRO/BATSE ²²	49503.5	121.6693 ± 0.0062	CGRO/BATSE ²²
49508.5	121.6771 ± 0.0042	CGRO/BATSE ²²	49513.5	121.7119 ± 0.0074	CGRO/BATSE ²²
49518.5	121.7488 ± 0.0057	CGRO/BATSE ²²	49523.5	121.7540 ± 0.0043	CGRO/BATSE ²²
49528.5	121.7890 ± 0.0038	CGRO/BATSE ²²	49533.5	121.8093 ± 0.0038	CGRO/BATSE ²²

Table B.1. Pulse period measurements of GX 1+4 (continued).

MJD	P_{spin} (s)	Instrument	MJD	P_{spin} (s)	Instrument
49538.5	121.8352 ± 0.0029	CGRO/BATSE ²²	49548.5	121.8701 ± 0.0030	CGRO/BATSE ²²
49558.5	121.9098 ± 0.0022	CGRO/BATSE ²²	49563.5	121.9172 ± 0.0016	CGRO/BATSE ²²
49573.5	121.9533 ± 0.0027	CGRO/BATSE ²²	49578.5	121.9681 ± 0.0036	CGRO/BATSE ²²
49583.5	121.9783 ± 0.0029	CGRO/BATSE ²²	49588.5	121.9839 ± 0.0031	CGRO/BATSE ²²
49593.5	121.9993 ± 0.0046	CGRO/BATSE ²²	49598.5	122.0037 ± 0.0033	CGRO/BATSE ²²
49603.5	122.0168 ± 0.0034	CGRO/BATSE ²²	49608.5	122.0263 ± 0.0023	CGRO/BATSE ²²
49613.5	122.0425 ± 0.0025	CGRO/BATSE ²²	49618.5	122.0517 ± 0.0019	CGRO/BATSE ²²
49623.5	122.0657 ± 0.0018	CGRO/BATSE ²²	49628.5	122.0727 ± 0.0025	CGRO/BATSE ²²
49633.5	122.0869 ± 0.0019	CGRO/BATSE ²²	49638.5	122.0986 ± 0.0014	CGRO/BATSE ²²
49643.5	122.1063 ± 0.0014	CGRO/BATSE ²²	49648.5	122.1128 ± 0.0014	CGRO/BATSE ²²
49653.5	122.1176 ± 0.0014	CGRO/BATSE ²²	49658.5	122.1159 ± 0.0012	CGRO/BATSE ²²
49663.5	122.1039 ± 0.0012	CGRO/BATSE ²²	49668.5	122.0851 ± 0.0012	CGRO/BATSE ²²
49673.5	122.0689 ± 0.0012	CGRO/BATSE ²²	49678.5	122.0477 ± 0.0011	CGRO/BATSE ²²
49683.5	122.0290 ± 0.0010	CGRO/BATSE ²²	49688.5	122.0089 ± 0.0010	CGRO/BATSE ²²
49693.5	121.9882 ± 0.0011	CGRO/BATSE ²²	49698.5	121.9674 ± 0.0013	CGRO/BATSE ²²
49703.5	121.9506 ± 0.0012	CGRO/BATSE ²²	49708.5	121.9345 ± 0.0012	CGRO/BATSE ²²
49713.5	121.9157 ± 0.0012	CGRO/BATSE ²²	49718.5	121.8965 ± 0.0012	CGRO/BATSE ²²
49723.5	121.8798 ± 0.0012	CGRO/BATSE ²²	49728.5	121.8653 ± 0.0011	CGRO/BATSE ²²
49733.5	121.8524 ± 0.0010	CGRO/BATSE ²²	49738.5	121.8382 ± 0.0009	CGRO/BATSE ²²
49743.5	121.8264 ± 0.0013	CGRO/BATSE ²²	49748.5	121.8116 ± 0.0013	CGRO/BATSE ²²
49753.5	121.8013 ± 0.0014	CGRO/BATSE ²²	49758.5	121.7929 ± 0.0015	CGRO/BATSE ²²
49763.5	121.7853 ± 0.0015	CGRO/BATSE ²²	49768.5	121.7783 ± 0.0011	CGRO/BATSE ²²
49773.5	121.7763 ± 0.0011	CGRO/BATSE ²²	49778.5	121.7751 ± 0.0015	CGRO/BATSE ²²
49783.5	121.7749 ± 0.0012	CGRO/BATSE ²²	49788.5	121.7792 ± 0.0012	CGRO/BATSE ²²
49793.5	121.7886 ± 0.0013	CGRO/BATSE ²²	49798.5	121.7998 ± 0.0017	CGRO/BATSE ²²
49803.5	121.8107 ± 0.0019	CGRO/BATSE ²²	49808.5	121.8269 ± 0.0028	CGRO/BATSE ²²
49813.5	121.8397 ± 0.0045	CGRO/BATSE ²²	49818.5	121.8633 ± 0.0069	CGRO/BATSE ²²
49823.5	121.9408 ± 0.0066	CGRO/BATSE ²²	49833.5	122.0374 ± 0.0024	CGRO/BATSE ²²
49838.5	122.1106 ± 0.0017	CGRO/BATSE ²²	49843.5	122.1481 ± 0.0045	CGRO/BATSE ²²
49848.5	122.1751 ± 0.0020	CGRO/BATSE ²²	49853.5	122.2054 ± 0.0019	CGRO/BATSE ²²
49858.5	122.2373 ± 0.0017	CGRO/BATSE ²²	49863.5	122.2816 ± 0.0021	CGRO/BATSE ²²
49868.5	122.3200 ± 0.0017	CGRO/BATSE ²²	49873.5	122.3576 ± 0.0030	CGRO/BATSE ²²
49878.5	122.3916 ± 0.0029	CGRO/BATSE ²²	49883.5	122.4229 ± 0.0017	CGRO/BATSE ²²
49888.5	122.4551 ± 0.0015	CGRO/BATSE ²²	49893.5	122.4858 ± 0.0017	CGRO/BATSE ²²
49898.5	122.5197 ± 0.0021	CGRO/BATSE ²²	49903.5	122.5389 ± 0.0022	CGRO/BATSE ²²
49908.5	122.5647 ± 0.0016	CGRO/BATSE ²²	49913.5	122.5870 ± 0.0017	CGRO/BATSE ²²
49918.5	122.6001 ± 0.0018	CGRO/BATSE ²²	49923.5	122.6279 ± 0.0016	CGRO/BATSE ²²
49928.5	122.6701 ± 0.0019	CGRO/BATSE ²²	49933.5	122.6951 ± 0.0014	CGRO/BATSE ²²
49938.5	122.7172 ± 0.0016	CGRO/BATSE ²²	49943.5	122.7428 ± 0.0022	CGRO/BATSE ²²
49948.5	122.7698 ± 0.0036	CGRO/BATSE ²²	49953.5	122.7684 ± 0.0015	CGRO/BATSE ²²
49958.5	122.7916 ± 0.0016	CGRO/BATSE ²²	49963.5	122.8126 ± 0.0014	CGRO/BATSE ²²
49968.5	122.8554 ± 0.0019	CGRO/BATSE ²²	49971.0	122.8770 ± 0.0210	GRANAT/SIGMA ²³
49973.5	122.8844 ± 0.0021	CGRO/BATSE ²²	49978.0	122.9230 ± 0.0090	GRANAT/SIGMA ²³
49978.5	122.9032 ± 0.0013	CGRO/BATSE ²²	49979.0	122.9420 ± 0.0400	GRANAT/SIGMA ²³
49983.5	122.9475 ± 0.0015	CGRO/BATSE ²²	49988.5	122.9744 ± 0.0017	CGRO/BATSE ²²
49993.5	122.9989 ± 0.0016	CGRO/BATSE ²²	49998.5	123.0159 ± 0.0015	CGRO/BATSE ²²
50003.5	123.0368 ± 0.0013	CGRO/BATSE ²²	50008.5	123.0714 ± 0.0017	CGRO/BATSE ²²
50013.5	123.1171 ± 0.0015	CGRO/BATSE ²²	50018.5	123.1516 ± 0.0017	CGRO/BATSE ²²
50023.5	123.1751 ± 0.0015	CGRO/BATSE ²²	50028.5	123.2126 ± 0.0016	CGRO/BATSE ²²
50033.5	123.2422 ± 0.0017	CGRO/BATSE ²²	50038.5	123.2704 ± 0.0016	CGRO/BATSE ²²
50043.5	123.2900 ± 0.0013	CGRO/BATSE ²²	50048.5	123.3110 ± 0.0013	CGRO/BATSE ²²
50053.5	123.3342 ± 0.0017	CGRO/BATSE ²²	50058.5	123.3476 ± 0.0014	CGRO/BATSE ²²
50063.5	123.3717 ± 0.0015	CGRO/BATSE ²²	50068.5	123.3866 ± 0.0018	CGRO/BATSE ²²
50073.5	123.4039 ± 0.0013	CGRO/BATSE ²²	50078.5	123.4371 ± 0.0018	CGRO/BATSE ²²
50083.5	123.4610 ± 0.0023	CGRO/BATSE ²²	50088.5	123.4780 ± 0.0043	CGRO/BATSE ²²
50093.5	123.4832 ± 0.0013	CGRO/BATSE ²²	50098.5	123.5011 ± 0.0016	CGRO/BATSE ²²
50103.5	123.5105 ± 0.0022	CGRO/BATSE ²²	50108.5	123.5284 ± 0.0019	CGRO/BATSE ²²
50113.5	123.5490 ± 0.0014	CGRO/BATSE ²²	50118.5	123.5799 ± 0.0015	CGRO/BATSE ²²
50123.5	123.6067 ± 0.0018	CGRO/BATSE ²²	50128.5	123.6319 ± 0.0014	CGRO/BATSE ²²
50133.5	123.6635 ± 0.0015	CGRO/BATSE ²²	50138.5	123.6869 ± 0.0014	CGRO/BATSE ²²
50143.5	123.7167 ± 0.0013	CGRO/BATSE ²²	50148.5	123.7418 ± 0.0014	CGRO/BATSE ²²
50153.5	123.7545 ± 0.0012	CGRO/BATSE ²²	50158.5	123.7712 ± 0.0013	CGRO/BATSE ²²
50162.0	123.7780 ± 0.0120	GRANAT/SIGMA ²³	50163.5	123.8032 ± 0.0013	CGRO/BATSE ²²
50164.0	123.8020 ± 0.0150	GRANAT/SIGMA ²³	50167.0	123.8060 ± 0.0160	GRANAT/SIGMA ²³
50168.0	123.8250 ± 0.0200	GRANAT/SIGMA ²³	50168.5	123.8367 ± 0.0015	CGRO/BATSE ²²

Table B.1. Pulse period measurements of GX 1+4 (continued).

MJD	P_{spin} (s)	Instrument	MJD	P_{spin} (s)	Instrument
50172.0	123.8590 ± 0.1300	GRANAT/SIGMA ²³	50173.5	123.8581 ± 0.0014	CGRO/BATSE ²²
50178.5	123.8745 ± 0.0015	CGRO/BATSE ²²	50183.5	123.8930 ± 0.0017	CGRO/BATSE ²²
50188.5	123.9078 ± 0.0014	CGRO/BATSE ²²	50193.5	123.9222 ± 0.0017	CGRO/BATSE ²²
50198.5	123.9417 ± 0.0012	CGRO/BATSE ²²	50203.5	123.9589 ± 0.0015	CGRO/BATSE ²²
50208.5	123.9910 ± 0.0013	CGRO/BATSE ²²	50213.5	124.0170 ± 0.0019	CGRO/BATSE ²²
50218.5	124.0544 ± 0.0012	CGRO/BATSE ²²	50223.5	124.0866 ± 0.0014	CGRO/BATSE ²²
50228.5	124.1055 ± 0.0013	CGRO/BATSE ²²	50233.5	124.1264 ± 0.0011	CGRO/BATSE ²²
50238.5	124.1540 ± 0.0022	CGRO/BATSE ²²	50243.5	124.1762 ± 0.0022	CGRO/BATSE ²²
50248.5	124.1898 ± 0.0039	CGRO/BATSE ²²	50288.5	124.3753 ± 0.0052	CGRO/BATSE ²²
50293.5	124.3888 ± 0.0030	CGRO/BATSE ²²	50298.5	124.3989 ± 0.0011	CGRO/BATSE ²²
50303.5	124.3883 ± 0.0009	CGRO/BATSE ²²	50308.5	124.3946 ± 0.0011	CGRO/BATSE ²²
50313.0	124.4040 ± 0.0030	BeppoSAX ²⁴	50313.5	124.4070 ± 0.0015	CGRO/BATSE ²²
50418.5	124.9810 ± 0.0057	CGRO/BATSE ²²	50423.5	125.0238 ± 0.0035	CGRO/BATSE ²²
50428.5	125.0702 ± 0.0031	CGRO/BATSE ²²	50438.5	125.1725 ± 0.0033	CGRO/BATSE ²²
50448.5	125.2853 ± 0.0030	CGRO/BATSE ²²	50453.5	125.3332 ± 0.0021	CGRO/BATSE ²²
50458.5	125.3840 ± 0.0019	CGRO/BATSE ²²	50463.5	125.4389 ± 0.0025	CGRO/BATSE ²²
50467.9	125.4870 ± 0.0022	CGRO/BATSE ²⁹	50475.9	125.5610 ± 0.0024	CGRO/BATSE ²⁹
50519.9	125.9130 ± 0.0024	CGRO/BATSE ²⁹	50532.0	126.0180 ± 0.0080	BeppoSAX/LECs,MECs,PDS ²⁴
50536.5	126.0380 ± 0.0021	CGRO/BATSE ²⁹	50539.7	126.0660 ± 0.0021	CGRO/BATSE ²⁹
50544.0	126.1150 ± 0.0020	CGRO/BATSE ²⁹	50567.9	126.2750 ± 0.0020	CGRO/BATSE ²⁹
50572.0	126.3020 ± 0.0030	CGRO/BATSE ²⁹	50580.0	126.3730 ± 0.0030	CGRO/BATSE ²⁹
50584.1	126.4040 ± 0.0009	CGRO/BATSE ²⁹	50588.0	126.4540 ± 0.0009	CGRO/BATSE ²⁹
50592.1	126.5140 ± 0.0007	CGRO/BATSE ²⁹	50595.6	126.5630 ± 0.0007	CGRO/BATSE ²⁹
50599.9	126.6010 ± 0.0020	CGRO/BATSE ²⁹	50604.3	126.6410 ± 0.0020	CGRO/BATSE ²⁹
50607.9	126.6690 ± 0.0021	CGRO/BATSE ²⁹	50616.0	126.7560 ± 0.0021	CGRO/BATSE ²⁹
50620.0	126.8060 ± 0.0012	CGRO/BATSE ²⁹	50624.1	126.8470 ± 0.0012	CGRO/BATSE ²⁹
50628.0	126.8850 ± 0.0022	CGRO/BATSE ²⁹	50632.0	126.9350 ± 0.0022	CGRO/BATSE ²⁹
50636.0	126.9590 ± 0.0006	CGRO/BATSE ²⁹	50640.0	126.9740 ± 0.0006	CGRO/BATSE ²⁹
50643.8	126.9800 ± 0.0007	CGRO/BATSE ²⁹	50648.0	127.0000 ± 0.0007	CGRO/BATSE ²⁹
50652.0	127.0170 ± 0.0006	CGRO/BATSE ²⁹	50656.0	127.0390 ± 0.0006	CGRO/BATSE ²⁹
50660.0	127.0550 ± 0.0005	CGRO/BATSE ²⁹	50663.9	127.0650 ± 0.0005	CGRO/BATSE ²⁹
50668.0	127.0850 ± 0.0007	CGRO/BATSE ²⁹	50672.2	127.0990 ± 0.0007	CGRO/BATSE ²⁹
50676.0	127.1150 ± 0.0007	CGRO/BATSE ²⁹	50680.0	127.1350 ± 0.0007	CGRO/BATSE ²⁹
50684.0	127.1420 ± 0.0012	CGRO/BATSE ²⁹	50688.0	127.1770 ± 0.0012	CGRO/BATSE ²⁹
50692.0	127.1810 ± 0.0022	CGRO/BATSE ²⁹	50704.0	127.2630 ± 0.0022	CGRO/BATSE ²⁹
50708.0	127.2850 ± 0.0027	CGRO/BATSE ²⁹	50720.0	127.3670 ± 0.0027	CGRO/BATSE ²⁹
50724.0	127.3660 ± 0.0024	CGRO/BATSE ²⁹	50728.0	127.3800 ± 0.0024	CGRO/BATSE ²⁹
50732.0	127.4080 ± 0.0020	CGRO/BATSE ²⁹	50768.0	127.5600 ± 0.0020	CGRO/BATSE ²⁹
50772.1	127.5710 ± 0.0019	CGRO/BATSE ²⁹	50776.0	127.5770 ± 0.0019	CGRO/BATSE ²⁹
50780.0	127.5870 ± 0.0011	CGRO/BATSE ²⁹	50784.0	127.5970 ± 0.0011	CGRO/BATSE ²⁹
50788.0	127.6060 ± 0.0014	CGRO/BATSE ²⁹	50791.9	127.6150 ± 0.0014	CGRO/BATSE ²⁹
50795.9	127.6210 ± 0.0011	CGRO/BATSE ²⁹	50800.0	127.6280 ± 0.0011	CGRO/BATSE ²⁹
50804.0	127.6370 ± 0.0010	CGRO/BATSE ²⁹	50808.0	127.6450 ± 0.0010	CGRO/BATSE ²⁹
50812.0	127.6520 ± 0.0011	CGRO/BATSE ²⁹	50816.1	127.6570 ± 0.0011	CGRO/BATSE ²⁹
50820.1	127.6680 ± 0.0014	CGRO/BATSE ²⁹	50824.1	127.6750 ± 0.0014	CGRO/BATSE ²⁹
50828.1	127.6830 ± 0.0015	CGRO/BATSE ²⁹	50832.0	127.6910 ± 0.0015	CGRO/BATSE ²⁹
50835.9	127.6970 ± 0.0013	CGRO/BATSE ²⁹	50839.9	127.7030 ± 0.0013	CGRO/BATSE ²⁹
50844.0	127.7080 ± 0.0012	CGRO/BATSE ²⁹	50847.9	127.7180 ± 0.0012	CGRO/BATSE ²⁹
50852.0	127.7250 ± 0.0013	CGRO/BATSE ²⁹	50856.0	127.7320 ± 0.0013	CGRO/BATSE ²⁹
50860.0	127.7370 ± 0.0018	CGRO/BATSE ²⁹	50864.1	127.7470 ± 0.0018	CGRO/BATSE ²⁹
50868.1	127.7520 ± 0.0024	CGRO/BATSE ²⁹	50872.0	127.7530 ± 0.0024	CGRO/BATSE ²⁹
50876.0	127.7830 ± 0.0021	CGRO/BATSE ²⁹	50880.1	127.7690 ± 0.0021	CGRO/BATSE ²⁹
50884.1	127.7710 ± 0.0029	CGRO/BATSE ²⁹	50887.9	127.7820 ± 0.0029	CGRO/BATSE ²⁹
50900.0	127.7960 ± 0.0019	CGRO/BATSE ²⁹	50916.0	127.8070 ± 0.0019	CGRO/BATSE ²⁹
50920.1	127.8120 ± 0.0073	CGRO/BATSE ²⁹	50924.0	127.8150 ± 0.0073	CGRO/BATSE ²⁹
50928.0	127.8120 ± 0.0020	CGRO/BATSE ²⁹	50932.0	127.8100 ± 0.0020	CGRO/BATSE ²⁹
50935.9	127.8070 ± 0.0014	CGRO/BATSE ²⁹	50940.0	127.8060 ± 0.0014	CGRO/BATSE ²⁹
50944.0	127.7960 ± 0.0009	CGRO/BATSE ²⁹	50948.0	127.7890 ± 0.0009	CGRO/BATSE ²⁹
50951.9	127.7850 ± 0.0015	CGRO/BATSE ²⁹	50959.9	127.7770 ± 0.0015	CGRO/BATSE ²⁹
50964.1	127.8110 ± 0.0015	CGRO/BATSE ²⁹	50968.0	127.8420 ± 0.0015	CGRO/BATSE ²⁹
50972.0	127.8710 ± 0.0011	CGRO/BATSE ²⁹	50976.0	127.9080 ± 0.0011	CGRO/BATSE ²⁹
50980.0	127.9390 ± 0.0007	CGRO/BATSE ²⁹	50984.0	127.9730 ± 0.0007	CGRO/BATSE ²⁹
50988.0	128.0080 ± 0.0006	CGRO/BATSE ²⁹	50992.1	128.0420 ± 0.0006	CGRO/BATSE ²⁹
50996.0	128.0750 ± 0.0007	CGRO/BATSE ²⁹	50999.5	128.1000 ± 0.0007	CGRO/BATSE ²⁹
51004.8	128.1520 ± 0.0015	CGRO/BATSE ²⁹	51008.0	128.1780 ± 0.0015	CGRO/BATSE ²⁹

Table B.1. Pulse period measurements of GX 1+4 (continued).

MJD	P_{spin} (s)	Instrument	MJD	P_{spin} (s)	Instrument
51012.1	128.2140 ± 0.0007	CGRO/BATSE ²⁹	51016.0	128.2520 ± 0.0007	CGRO/BATSE ²⁹
51020.1	128.2880 ± 0.0007	CGRO/BATSE ²⁹	51023.9	128.3210 ± 0.0007	CGRO/BATSE ²⁹
51028.0	128.3560 ± 0.0007	CGRO/BATSE ²⁹	51032.0	128.3920 ± 0.0007	CGRO/BATSE ²⁹
51036.0	128.4270 ± 0.0006	CGRO/BATSE ²⁹	51040.0	128.4640 ± 0.0006	CGRO/BATSE ²⁹
51044.0	128.5010 ± 0.0004	CGRO/BATSE ²⁹	51046.6	128.5250 ± 0.0004	CGRO/BATSE ²⁹
51047.8	128.5442 ± 0.0107	BeppoSAX/WFC ²⁵	51052.9	128.5840 ± 0.0008	CGRO/BATSE ²⁹
51056.0	128.6140 ± 0.0008	CGRO/BATSE ²⁹	51057.8	128.6338 ± 0.0053	BeppoSAX/WFC ²⁵
51060.1	128.6530 ± 0.0005	CGRO/BATSE ²⁹	51063.9	128.6920 ± 0.0005	CGRO/BATSE ²⁹
51067.2	128.7238 ± 0.0049	BeppoSAX/WFC ²⁵	51068.0	128.7300 ± 0.0004	CGRO/BATSE ²⁹
51072.1	128.7680 ± 0.0004	CGRO/BATSE ²⁹	51075.9	128.8050 ± 0.0004	CGRO/BATSE ²⁹
51079.8	128.8410 ± 0.0004	CGRO/BATSE ²⁹	51079.2	128.8189 ± 0.0127	BeppoSAX/WFC ²⁵
51084.0	128.8820 ± 0.0003	CGRO/BATSE ²⁹	51084.6	128.8474 ± 0.0240	BeppoSAX/WFC ²⁵
51088.0	128.9190 ± 0.0003	CGRO/BATSE ²⁹	51092.0	128.9570 ± 0.0003	CGRO/BATSE ²⁹
51092.3	128.9581 ± 0.0033	BeppoSAX/WFC ²⁵	51096.0	128.9920 ± 0.0003	CGRO/BATSE ²⁹
51099.9	129.0240 ± 0.0002	CGRO/BATSE ²⁹	51103.8	129.0580 ± 0.0002	CGRO/BATSE ²⁹
51107.9	129.0890 ± 0.0006	CGRO/BATSE ²⁹	51112.0	129.1230 ± 0.0006	CGRO/BATSE ²⁹
51116.0	129.1520 ± 0.0008	CGRO/BATSE ²⁹	51120.1	129.1840 ± 0.0008	CGRO/BATSE ²⁹
51124.0	129.2150 ± 0.0010	CGRO/BATSE ²⁹	51128.1	129.2460 ± 0.0010	CGRO/BATSE ²⁹
51132.0	129.2780 ± 0.0008	CGRO/BATSE ²⁹	51136.1	129.3100 ± 0.0008	CGRO/BATSE ²⁹
51139.9	129.3420 ± 0.0008	CGRO/BATSE ²⁹	51144.1	129.3740 ± 0.0008	CGRO/BATSE ²⁹
51147.9	129.4040 ± 0.0008	CGRO/BATSE ²⁹	51152.0	129.4420 ± 0.0008	CGRO/BATSE ²⁹
51156.0	129.4770 ± 0.0005	CGRO/BATSE ²⁹	51160.0	129.5110 ± 0.0005	CGRO/BATSE ²⁹
51163.8	129.5450 ± 0.0009	CGRO/BATSE ²⁹	51168.0	129.5790 ± 0.0009	CGRO/BATSE ²⁹
51172.0	129.6100 ± 0.0008	CGRO/BATSE ²⁹	51176.0	129.6470 ± 0.0008	CGRO/BATSE ²⁹
51180.0	129.6830 ± 0.0008	CGRO/BATSE ²⁹	51184.0	129.7190 ± 0.0008	CGRO/BATSE ²⁹
51188.1	129.7520 ± 0.0007	CGRO/BATSE ²⁹	51192.0	129.7870 ± 0.0007	CGRO/BATSE ²⁹
51196.1	129.8230 ± 0.0008	CGRO/BATSE ²⁹	51200.0	129.8580 ± 0.0008	CGRO/BATSE ²⁹
51204.0	129.8940 ± 0.0005	CGRO/BATSE ²⁹	51208.0	129.9310 ± 0.0005	CGRO/BATSE ²⁹
51212.0	129.9650 ± 0.0005	CGRO/BATSE ²⁹	51216.0	130.0030 ± 0.0005	CGRO/BATSE ²⁹
51219.9	130.0370 ± 0.0005	CGRO/BATSE ²⁹	51224.0	130.0750 ± 0.0005	CGRO/BATSE ²⁹
51228.0	130.1120 ± 0.0005	CGRO/BATSE ²⁹	51230.3	130.1523 ± 0.0074	BeppoSAX/WFC ²⁵
51232.0	130.1530 ± 0.0005	CGRO/BATSE ²⁹	51236.1	130.1930 ± 0.0005	CGRO/BATSE ²⁹
51240.0	130.2320 ± 0.0005	CGRO/BATSE ²⁹	51244.1	130.2730 ± 0.0004	CGRO/BATSE ²⁹
51248.1	130.3150 ± 0.0004	CGRO/BATSE ²⁹	51249.4	130.3295 ± 0.0140	BeppoSAX/WFC ²⁵
51251.9	130.3560 ± 0.0004	CGRO/BATSE ²⁹	51256.0	130.3990 ± 0.0004	CGRO/BATSE ²⁹
51259.9	130.4410 ± 0.0003	CGRO/BATSE ²⁹	51262.5	130.4689 ± 0.0131	BeppoSAX/WFC ²⁵
51263.9	130.4880 ± 0.0003	CGRO/BATSE ²⁹	51267.9	130.5330 ± 0.0003	CGRO/BATSE ²⁹
51270.8	130.5625 ± 0.0074	BeppoSAX/WFC ²⁵	51272.0	130.5780 ± 0.0003	CGRO/BATSE ²⁹
51274.7	130.6058 ± 0.0099	BeppoSAX/WFC ²⁵	51276.1	130.6250 ± 0.0003	CGRO/BATSE ²⁹
51278.5	130.6510 ± 0.0047	BeppoSAX/WFC ²⁵	51280.1	130.6720 ± 0.0003	CGRO/BATSE ²⁹
51284.1	130.7200 ± 0.0003	CGRO/BATSE ²⁹	51288.0	130.7660 ± 0.0003	CGRO/BATSE ²⁹
51292.0	130.8130 ± 0.0002	CGRO/BATSE ²⁹	51296.1	130.8590 ± 0.0002	CGRO/BATSE ²⁹
51300.1	130.9050 ± 0.0002	CGRO/BATSE ²⁹	51304.0	130.9530 ± 0.0002	CGRO/BATSE ²⁹
51308.0	130.9990 ± 0.0002	CGRO/BATSE ²⁹	51312.0	131.0450 ± 0.0002	CGRO/BATSE ²⁹
51315.9	131.0910 ± 0.0003	CGRO/BATSE ²⁹	51320.0	131.1390 ± 0.0003	CGRO/BATSE ²⁹
51324.0	131.1850 ± 0.0003	CGRO/BATSE ²⁹	51328.0	131.2280 ± 0.0003	CGRO/BATSE ²⁹
51332.0	131.2740 ± 0.0003	CGRO/BATSE ²⁹	51336.0	131.3210 ± 0.0003	CGRO/BATSE ²⁹
51340.0	131.3650 ± 0.0004	CGRO/BATSE ²⁹	51344.0	131.4090 ± 0.0004	CGRO/BATSE ²⁹
51460.9	132.5723 ± 0.0089	BeppoSAX/WFC ²⁵	51464.3	132.6220 ± 0.0174	BeppoSAX/WFC ²⁵
51785.0	134.9256 ± 0.0010	BeppoSAX ²⁴	52346.1	137.4690 ± 0.3680	RXTE/PCA&HEXTE ²⁶
52351.3	137.2540 ± 0.2910	RXTE/PCA&HEXTE ²⁶	52359.9	137.7750 ± 0.0920	RXTE/PCA&HEXTE ²⁶
52366.6	137.9440 ± 0.2760	RXTE/PCA&HEXTE ²⁶	52384.7	137.8050 ± 0.1690	RXTE/PCA&HEXTE ²⁶
52392.3	137.9580 ± 0.1840	RXTE/PCA&HEXTE ²⁶	52401.2	137.8650 ± 0.2000	RXTE/PCA&HEXTE ²⁶
52407.0	137.6350 ± 0.1840	RXTE/PCA&HEXTE ²⁶	52418.0	138.0180 ± 0.2610	RXTE/PCA&HEXTE ²⁶
52422.0	137.1890 ± 0.2910	RXTE/PCA&HEXTE ²⁶	52431.2	138.2020 ± 0.4760	RXTE/PCA&HEXTE ²⁶
52434.9	138.0790 ± 0.1990	RXTE/PCA&HEXTE ²⁶	52450.8	137.5860 ± 1.8740	RXTE/PCA&HEXTE ²⁶
52466.1	137.1250 ± 0.3070	RXTE/PCA&HEXTE ²⁶	52470.7	137.9390 ± 0.1840	RXTE/PCA&HEXTE ²⁶
52490.9	138.1370 ± 0.2300	RXTE/PCA&HEXTE ²⁶	52491.0	138.1700 ± 0.0010	Chandra&RXTE ²⁷
52493.0	138.1680 ± 0.1230	RXTE/PCA&HEXTE ²⁶	52499.2	138.1060 ± 0.1690	RXTE/PCA&HEXTE ²⁶
52502.2	138.1060 ± 0.5530	RXTE/PCA&HEXTE ²⁶	52503.5	138.2590 ± 0.8450	RXTE/PCA&HEXTE ²⁶
52512.6	138.7040 ± 0.4150	RXTE/PCA&HEXTE ²⁶	52515.7	138.3350 ± 0.1850	RXTE/PCA&HEXTE ²⁶
52521.8	138.3660 ± 0.4610	RXTE/PCA&HEXTE ²⁶	52526.1	138.3960 ± 0.4920	RXTE/PCA&HEXTE ²⁶
52528.9	138.0580 ± 0.6760	RXTE/PCA&HEXTE ²⁶	52535.0	138.1350 ± 0.2610	RXTE/PCA&HEXTE ²⁶
52539.6	138.4570 ± 0.3840	RXTE/PCA&HEXTE ²⁶	52542.3	138.1650 ± 0.6450	RXTE/PCA&HEXTE ²⁶
52548.4	137.9960 ± 0.5680	RXTE/PCA&HEXTE ²⁶	52555.5	138.0570 ± 3.2090	RXTE/PCA&HEXTE ²⁶

Table B.1. Pulse period measurements of GX 1+4 (continued).

MJD	$P_{spin}(s)$	Instrument	MJD	$P_{spin}(s)$	Instrument
52561.0	138.0570 ± 1.5660	RXTE/PCA&HEXTE ²⁶	52565.6	138.1180 ± 0.7980	RXTE/PCA&HEXTE ²⁶
52582.1	138.1630 ± 0.4920	RXTE/PCA&HEXTE ²⁶	52585.8	138.6700 ± 0.2910	RXTE/PCA&HEXTE ²⁶
52589.2	138.6230 ± 0.1080	RXTE/PCA&HEXTE ²⁶	52591.9	138.5770 ± 0.2000	RXTE/PCA&HEXTE ²⁶
52594.1	138.4850 ± 0.0920	RXTE/PCA&HEXTE ²⁶	52917.6	139.6300 ± 0.0060	INTEGRAL ²⁸
53052.1	140.6132 ± 0.0002	INTEGRAL ²⁸	53252.4	141.5649 ± 0.0001	INTEGRAL ²⁸
53422.0	141.3310 ± 0.3380	INTEGRAL/ISGRI ²⁵	53431.0	140.9101 ± 0.5285	INTEGRAL/ISGRI ²⁵
53434.0	141.3730 ± 0.2320	INTEGRAL/ISGRI ²⁵	53464.0	141.8630 ± 0.2986	INTEGRAL/ISGRI ²⁵
53467.0	141.6670 ± 0.1540	INTEGRAL/ISGRI ²⁵	53470.0	141.4530 ± 0.2489	INTEGRAL/ISGRI ²⁵
53473.0	141.5861 ± 0.3421	INTEGRAL/ISGRI ²⁵	53476.0	141.6270 ± 0.1014	INTEGRAL/ISGRI ²⁵
53479.0	141.8120 ± 0.1796	INTEGRAL/ISGRI ²⁵	53611.0	142.9630 ± 0.2911	INTEGRAL/ISGRI ²⁵
53620.0	142.9510 ± 0.3223	INTEGRAL/ISGRI ²⁵	53635.0	142.8820 ± 0.1238	INTEGRAL/ISGRI ²⁵
53638.0	143.1800 ± 0.1695	INTEGRAL/ISGRI ²⁵	53641.0	143.0350 ± 0.2270	INTEGRAL/ISGRI ²⁵
53644.0	143.0580 ± 0.2625	INTEGRAL/ISGRI ²⁵	53647.0	142.6760 ± 0.7286	INTEGRAL/ISGRI ²⁵
53650.0	142.9760 ± 0.3018	INTEGRAL/ISGRI ²⁵	53653.0	143.0450 ± 0.1820	INTEGRAL/ISGRI ²⁵
53656.0	143.1370 ± 0.2403	INTEGRAL/ISGRI ²⁵	53659.0	143.1670 ± 0.2502	INTEGRAL/ISGRI ²⁵
53662.0	143.2370 ± 0.1376	INTEGRAL/ISGRI ²⁵	53665.0	143.2250 ± 0.2702	INTEGRAL/ISGRI ²⁵
53668.0	143.0780 ± 0.1641	INTEGRAL/ISGRI ²⁵	53776.0	143.7540 ± 0.4973	INTEGRAL/ISGRI ²⁵
53779.0	143.8440 ± 0.1433	INTEGRAL/ISGRI ²⁵	53782.0	143.8710 ± 0.1307	INTEGRAL/ISGRI ²⁵
53785.0	143.8310 ± 0.1705	INTEGRAL/ISGRI ²⁵	53788.0	143.9010 ± 0.0930	INTEGRAL/ISGRI ²⁵
53791.0	143.9800 ± 0.0914	INTEGRAL/ISGRI ²⁵	53794.0	144.0310 ± 0.1641	INTEGRAL/ISGRI ²⁵
53797.0	144.0950 ± 0.2588	INTEGRAL/ISGRI ²⁵	53803.0	144.0920 ± 0.1138	INTEGRAL/ISGRI ²⁵
53806.0	144.2470 ± 0.1827	INTEGRAL/ISGRI ²⁵	53809.0	144.0340 ± 0.1718	INTEGRAL/ISGRI ²⁵
53812.0	144.1330 ± 0.1196	INTEGRAL/ISGRI ²⁵	53815.0	144.0920 ± 0.1236	INTEGRAL/ISGRI ²⁵
53818.0	144.5760 ± 0.2612	INTEGRAL/ISGRI ²⁵	53821.0	144.2650 ± 0.1599	INTEGRAL/ISGRI ²⁵
53830.0	144.2780 ± 0.1662	INTEGRAL/ISGRI ²⁵	53833.0	144.1490 ± 0.1517	INTEGRAL/ISGRI ²⁵
53836.0	144.2310 ± 0.2570	INTEGRAL/ISGRI ²⁵	53839.0	144.2210 ± 0.1294	INTEGRAL/ISGRI ²⁵
53842.0	144.4540 ± 0.1796	INTEGRAL/ISGRI ²⁵	53845.0	144.4040 ± 0.0892	INTEGRAL/ISGRI ²⁵
53965.0	145.3250 ± 0.2286	INTEGRAL/ISGRI ²⁵	53968.0	145.5370 ± 0.1574	INTEGRAL/ISGRI ²⁵
53974.0	145.4100 ± 0.1504	INTEGRAL/ISGRI ²⁵	53977.0	145.5250 ± 0.1218	INTEGRAL/ISGRI ²⁵
53980.0	145.4940 ± 0.1308	INTEGRAL/ISGRI ²⁵	53983.0	145.5390 ± 0.0991	INTEGRAL/ISGRI ²⁵
53986.0	145.5590 ± 0.0952	INTEGRAL/ISGRI ²⁵	53989.0	145.7140 ± 0.0863	INTEGRAL/ISGRI ²⁵
53992.0	145.7020 ± 0.0868	INTEGRAL/ISGRI ²⁵	53998.0	145.7880 ± 0.1160	INTEGRAL/ISGRI ²⁵
54001.0	145.6570 ± 0.1365	INTEGRAL/ISGRI ²⁵	54004.0	145.8051 ± 0.1143	INTEGRAL/ISGRI ²⁵
54010.0	145.9100 ± 0.0883	INTEGRAL/ISGRI ²⁵	54013.0	145.8280 ± 0.1115	INTEGRAL/ISGRI ²⁵
54022.0	145.8840 ± 0.0907	INTEGRAL/ISGRI ²⁵	54025.0	146.0170 ± 0.0638	INTEGRAL/ISGRI ²⁵
54028.0	146.1190 ± 0.0735	INTEGRAL/ISGRI ²⁵	54031.0	146.0260 ± 0.0850	INTEGRAL/ISGRI ²⁵
54034.0	146.0960 ± 0.0748	INTEGRAL/ISGRI ²⁵	54148.0	147.2450 ± 0.0681	INTEGRAL/ISGRI ²⁵
54151.0	147.3313 ± 0.0736	INTEGRAL/ISGRI ²⁵	54157.0	147.2670 ± 0.1061	INTEGRAL/ISGRI ²⁵
54160.0	147.2800 ± 0.0755	INTEGRAL/ISGRI ²⁵	54163.0	147.3790 ± 0.0746	INTEGRAL/ISGRI ²⁵
54166.0	147.4210 ± 0.0999	INTEGRAL/ISGRI ²⁵	54169.0	147.4370 ± 0.0758	INTEGRAL/ISGRI ²⁵
54175.0	147.5010 ± 0.0742	INTEGRAL/ISGRI ²⁵	54178.0	147.5084 ± 0.0693	INTEGRAL/ISGRI ²⁵
54187.0	147.6360 ± 0.0680	INTEGRAL/ISGRI ²⁵	54193.0	147.7020 ± 0.1296	INTEGRAL/ISGRI ²⁵
54196.0	147.7520 ± 0.0915	INTEGRAL/ISGRI ²⁵	54205.0	147.6560 ± 0.5624	INTEGRAL/ISGRI ²⁵
54208.0	148.0240 ± 0.1515	INTEGRAL/ISGRI ²⁵	54211.0	147.8410 ± 0.1414	INTEGRAL/ISGRI ²⁵
54214.0	147.9820 ± 0.0789	INTEGRAL/ISGRI ²⁵	54334.0	149.1250 ± 0.1883	INTEGRAL/ISGRI ²⁵
54337.0	149.2490 ± 0.1609	INTEGRAL/ISGRI ²⁵	54340.0	149.2190 ± 0.1271	INTEGRAL/ISGRI ²⁵
54346.0	149.2859 ± 0.1262	INTEGRAL/ISGRI ²⁵	54355.0	149.4520 ± 0.1408	INTEGRAL/ISGRI ²⁵
54358.0	149.2110 ± 0.1932	INTEGRAL/ISGRI ²⁵	54361.0	149.7855 ± 0.4506	INTEGRAL/ISGRI ²⁵
54364.0	149.5520 ± 0.4772	INTEGRAL/ISGRI ²⁵	54367.0	149.7460 ± 0.2236	INTEGRAL/ISGRI ²⁵
54370.0	149.3710 ± 0.1449	INTEGRAL/ISGRI ²⁵	54379.0	149.6473 ± 0.1996	INTEGRAL/ISGRI ²⁵
54388.0	149.7940 ± 0.1169	INTEGRAL/ISGRI ²⁵	54391.0	149.6390 ± 0.1620	INTEGRAL/ISGRI ²⁵
54541.0	150.5900 ± 0.3070	INTEGRAL/ISGRI ²⁵	54704.2	152.7987 ± 0.0017	Fermi/GBM ²⁵
54719.5	152.9342 ± 0.0027	Fermi/GBM ²⁵	54728.1	153.0133 ± 0.0037	Fermi/GBM ²⁵
54736.1	153.0986 ± 0.0024	Fermi/GBM ²⁵	54744.1	153.1724 ± 0.0018	Fermi/GBM ²⁵
54752.1	153.2497 ± 0.0031	Fermi/GBM ²⁵	54769.0	153.3928 ± 0.0030	Fermi/GBM ²⁵
54775.9	153.4629 ± 0.0016	Fermi/GBM ²⁵	54784.0	153.5438 ± 0.0012	Fermi/GBM ²⁵
54791.9	153.6298 ± 0.0012	Fermi/GBM ²⁵	54800.4	153.7102 ± 0.0024	Fermi/GBM ²⁵
54808.1	153.7824 ± 0.0025	Fermi/GBM ²⁵	54815.7	153.8466 ± 0.0021	Fermi/GBM ²⁵
54824.5	153.9263 ± 0.0010	Fermi/GBM ²⁵	54831.9	154.0113 ± 0.0007	Fermi/GBM ²⁵
54840.0	154.1071 ± 0.0007	Fermi/GBM ²⁵	54847.9	154.1913 ± 0.0011	Fermi/GBM ²⁵
54856.2	154.2690 ± 0.0022	Fermi/GBM ²⁵	54880.0	154.4594 ± 0.0030	Fermi/GBM ²⁵
54887.9	154.5198 ± 0.0023	Fermi/GBM ²⁵	54904.7	154.6587 ± 0.0032	Fermi/GBM ²⁵
54912.2	154.7181 ± 0.0020	Fermi/GBM ²⁵	54919.8	154.7824 ± 0.0020	Fermi/GBM ²⁵
54927.9	154.8590 ± 0.0024	Fermi/GBM ²⁵	54936.3	154.9303 ± 0.0016	Fermi/GBM ²⁵
54944.0	154.9999 ± 0.0016	Fermi/GBM ²⁵	54952.1	155.0761 ± 0.0021	Fermi/GBM ²⁵

Table B.1. Pulse period measurements of GX 1+4 (continued).

MJD	$P_{spin}(s)$	Instrument	MJD	$P_{spin}(s)$	Instrument
54959.5	155.1347 ± 0.0023	Fermi/GBM ²⁵	54968.0	155.2070 ± 0.0019	Fermi/GBM ²⁵
54975.9	155.2761 ± 0.0021	Fermi/GBM ²⁵	54984.0	155.3446 ± 0.0014	Fermi/GBM ²⁵
54992.0	155.4194 ± 0.0010	Fermi/GBM ²⁵	55000.0	155.4976 ± 0.0010	Fermi/GBM ²⁵
55007.9	155.5781 ± 0.0010	Fermi/GBM ²⁵	55016.1	155.6549 ± 0.0019	Fermi/GBM ²⁵
55023.9	155.7235 ± 0.0018	Fermi/GBM ²⁵	55031.9	155.7919 ± 0.0023	Fermi/GBM ²⁵
55040.0	155.8628 ± 0.0026	Fermi/GBM ²⁵	55047.9	155.9249 ± 0.0016	Fermi/GBM ²⁵
55056.0	156.0042 ± 0.0009	Fermi/GBM ²⁵	55063.8	156.0889 ± 0.0007	Fermi/GBM ²⁵
55072.3	156.1731 ± 0.0015	Fermi/GBM ²⁵	55079.8	156.2443 ± 0.0016	Fermi/GBM ²⁵
55087.9	156.3116 ± 0.0021	Fermi/GBM ²⁵	55120.0	156.5714 ± 0.0011	Fermi/GBM ²⁵
55128.1	156.6515 ± 0.0007	Fermi/GBM ²⁵	55135.9	156.7381 ± 0.0008	Fermi/GBM ²⁵
55143.9	156.8283 ± 0.0007	Fermi/GBM ²⁵	55151.9	156.9130 ± 0.0009	Fermi/GBM ²⁵
55159.9	157.0009 ± 0.0006	Fermi/GBM ²⁵	55168.0	157.0931 ± 0.0005	Fermi/GBM ²⁵
55176.0	157.1903 ± 0.0005	Fermi/GBM ²⁵	55184.2	157.2875 ± 0.0006	Fermi/GBM ²⁵
55191.9	157.3714 ± 0.0009	Fermi/GBM ²⁵	55200.0	157.4465 ± 0.0014	Fermi/GBM ²⁵
55207.9	157.5144 ± 0.0022	Fermi/GBM ²⁵	55224.0	157.6355 ± 0.0023	Fermi/GBM ²⁵
55232.0	157.7167 ± 0.0006	Fermi/GBM ²⁵	55237.5	157.7838 ± 0.0019	Fermi/GBM ²⁵

References. (1) Lewin et al. (1971); (2) White et al. (1976); (3) Koo & Haymes (1980); (4) Becker et al. (1976); (5) Doty et al. (1981); (6) Becker & White in Cutler et al. (1986); (7) Strickman et al. (1980); (8) Coe et al. (1981); (9) Kendziorra et al. (1982); (10) Elsner et al. (1985); (11) Ricketts et al. (1982); (12) Jayanthi et al. (1987) (Three probable periods centred at 108.8, 112.8, and 121.2 s were selected in this paper and they decided in favour of 120.6 s, but the trend indicates the best period is 108.8 s.); (13) Damle et al. (1988); (14) Leahy (1989); (15) Greenhill et al. (1993); (16) Makishima et al. (1988); (17) Mony et al. (1991); (18) Dotani et al. (1989); (19) Sakao et al. (1990); (20) Lutovinov et al. (1994); (21) Laurent et al. (1993); (22) Chakrabarty et al. (1997); (23) David et al. (1998); (24) Naik et al. (2005); (25) This work; (26) Cui & Smith (2004); (27) Paul et al. (2005); (28) Ferrigno et al. (2007), (29) BATSE Public Data Archive.